Chemical Science

ROYAL SOCIETY OF CHEMISTRY

REVIEW

View Article Online
View Journal | View Issue

Cite this: *Chem. Sci.*, 2024, **15**, 5061

Graphdiyne/metal oxide hybrid materials for efficient energy and environmental catalysis

Yuhua Zhu,[ac] Shuhong Zhang,[a] Xiaofeng Qiu,[a] Quanguo Hao,[a] Yan Wu,[a] Zhu Luo*[ab] and Yanbing Guo *[ab]

Received 3rd January 2024
Accepted 22nd February 2024

DOI: 10.1039/d4sc00036f

rsc.li/chemical-science

Graphdiyne (GDY)-based materials, owing to their unique structure and tunable electronic properties, exhibit great potential in the fields of catalysis, energy, environmental science, and beyond. In particular, GDY/metal oxide hybrid materials (GDY/MOs) have attracted extensive attention in energy and environmental catalysis. The interaction between GDY and metal oxides can increase the number of intrinsic active sites, facilitate charge transfer, and regulate the adsorption and desorption of intermediate species. In this review, we summarize the structure, synthesis, advanced characterization, small molecule activation mechanism and applications of GDY/MOs in energy conversion and environmental remediation. The intrinsic structure–activity relationship and corresponding reaction mechanism are highlighted. In particular, the activation mechanisms of reactant molecules (H_2O, O_2, N_2, *etc.*) on GDY/MOs are systemically discussed. Finally, we outline some new perspectives of opportunities and challenges in developing GDY/MOs for efficient energy and environmental catalysis.

1. Introduction

With the rapid development of human society and economy, the problems of energy crisis and environmental pollution have become increasingly prominent. Developing renewable energy sources and strengthening the control of pollutants are two effective strategies to solve the aforementioned problems.[1–4] Catalysts with high efficiency and low cost play a crucial role in addressing challenges.[5] Noble metal catalysts, including Pt, Pd, Ag, and Au, have been widely utilized due to their high catalytic performances.[2,4] However, noble metal catalysts still suffer from limited availability, prohibitive cost, and relatively low stability, which prompt the exploration of alternative catalytic materials. Carbon-based materials are attracting growing attention due to their distinctive advantages in terms of low cost, large specific surface area, as well as tunable electronic structures,[6–8] which exhibit potential applications in energy and environmental catalysis.

Different from traditional inorganic carbon materials (graphene, carbon nanotubes, *etc.*) and organic polymerized carbon materials (carbon nitride, covalent organic frameworks, *etc.*), with single sp^2 or sp^3 hybridized states, graphdiyne (GDY), a rising-star carbon allotrope, comprising sp and sp^2 hybridized carbon atoms, is an emerging two-dimensional (2D) planar carbon material.[9–11] GDY possesses well dispersed electron-rich cavities and a large π-conjunction structure, which endows it with unique chemical and physical properties, including an adjustable intrinsic bandgap, fast charge transfer, excellent conductivity and so on. The electron mobility of GDY is considerably higher than that of common organic polymerized carbon materials, even up to several orders of magnitude.[12–14] Moreover, the sp-hybridized carbon atoms and triangular cavities in the 2D GDY conjugated structure facilitate the formation of strong interfacial contacts with active components such as metal atoms and metal oxides.[15,16] The fabrication of a wide range of unique GDY-based materials expands the applications of GDY in energy catalysis, environmental remediation, energy storage, electronics, life sciences, and other fields.[17–20] In particular, GDY/MOs, through the interaction between GDY and metal oxides, enable the modulation of the electronic structure and increase the number of active sites, which improves the intrinsic activity, and enhances the stability.[21–25] Therefore, the GDY/MOs exhibit unique advantages in heterogeneous catalysis.

Recently, many excellent and interesting research studies about GDY/MOs were published. However, a thorough overview of GDY/MOs for efficient energy and environmental catalysis has not been reported. This review summarizes the applications of GDY/MOs in the field of energy and environmental catalysis, emphasizing the uniqueness of the intrinsic relationship between the structure and performance and the corresponding mechanism. The structure, synthesis, characterization and applications of GDY/MOs are fully introduced. In particular, the

[a]*Engineering Research Center of Photoenergy Utilization for Pollution Control and Carbon Reduction, Ministry of Education, College of Chemistry, Central China Normal University, Wuhan, Hubei 430082, China. E-mail: guoyanbing@mail.ccnu.edu.cn*

[b]*Wuhan Institute of Photochemistry and Technology, 7 North Bingang Road, Wuhan, Hubei 430082, China*

[c]*School of Civil Engineering, Wuhan University, Wuhan 430072, China*

activation behaviors on GDY/MOs for efficient energy and environmental catalysis, such as activation of H_2O, O_2 and N_2, are systemically discussed. Finally, we comprehensively discuss the existing key challenges and prospects for fundamental and applied research of GDY/MOs in the field of energy and environmental remediation.

2. Typical structure, synthesis and characterization of GDY/MOs

2.1 Typical structure of GDY/MOs

Because of the abundant sp conjugated diyne bonds and unique triangular pore structure, GDY is widely used as a good carrier of MOs in the field of catalysis.[11] Therefore, it is of great significance to study the unique structure of GDY/MOs. Herein, we summarize the structure of GDY/MOs as follows.

2.1.1 Sub-nanoclusters. Sub-nanoclusters are normally below 1 nm and consist of several atoms (Fig. 1a), which are related to but somewhat different from crystal nuclei with clear structures.[26,27] The sub-nanoclusters reduce the average coordination number of the metal atoms. And, the subcluster species have a smaller contact angle with the support, forming a layered structure, which contributes to enhancing the interaction between the metal atoms and support and increasing the stability of the sub-nanoclusters.[28] Usually, the interactions between sub-nanocluster MOs and GDY are chemical bonds rather than weaker forces such as van der Waals forces. Due to the small size of nanoclusters, the utilization of atoms at the GDY/MO interface is effectively improved, which can increase the amount of active sites.[11] Meanwhile, GDY and sub-nanocluster MOs can achieve efficient electron transfer through interfacial chemical bonding, promoting the adsorption and activation of reactant molecules. For instance, the unique sp hybrid carbon and copper sites at the interface of sub-nanoclusters CuO and GDY can provide electrons to the antibonding orbitals of adsorbed oxygen to form the $\cdot O_2^-$ through a bridge configuration, leading to low-temperature CO oxidation.[29]

2.1.2 Nanoparticles. Nanoparticles with sizes >1 nm usually have more than 40 atoms (Fig. 1b), which generally exhibit a well-defined crystal structure.[30] For GDY/MOs, the particle size of most MOs is nanometer, which is nanoparticle. The structures of GDY/MOs are mainly heterostructures. The heterostructured GDY/MOs can modulate the morphology of the MOs such as reducing the particle size of the MOs, forming oxygen vacancies, metal ion vacancies, *etc.*, which effectively promote the adsorption of reactant molecules and enhances the intrinsic activity of the GDY/MOs. For example, the interfacial sp hybrid C–O–Mo bond between GDY and MoO_3 promoted the formation of an amount of oxygen vacancies, greatly increased the number of H_2O adsorption sites, leading to excellent electrochemical hydrogen evolution performance.[22] In addition, the heterostructure of GDY/MOs can change the electronic structure, physical and chemical properties of the MOs, such as shortening the band gap and improving the electrical conductivity, which is conducive to promoting the electron transfer and mobility, and facilitating the activation of reactant molecules and the transformation of intermediate species. For example, the construction of heterostructured GDY/SnO_x increased the charge transfer ability and facilitated the conversion of key intermediates (OCHO* species), exhibiting CO_2 reduction reaction performance.[31] Therefore, the unique structure of GDY/MOs makes them show greater application prospects in the field of energy and environmental catalysis.

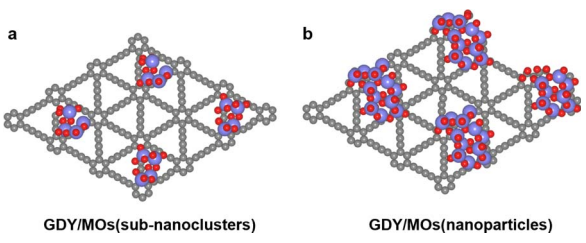

Fig. 1 Schematic structure of GDY/MOs: (a) MOs as sub-nanoclusters; (b) MOs as nanoparticles.

2.2 Synthesis of GDY/MOs

Metal oxides (MOs) have attracted wide attention in environmental and energy-related fields. In order to meet the different applications in these fields, it is of great significance to explore the controllable preparation and regulation of MOs. Recent studies have shown that the composite of carbon materials with MOs can modulate the structure of the MOs and thus enhance the catalytic activity and stability of MOs. Theoretical predictions demonstrated that the triangular cavities with the edges of sp-hybridized carbon atoms in the GDY would have a much stronger binding energy with many elements (for example, Li, K, and Ti) than the prevailing sp^2-hybridized carbon materials.[32–34] This particular interaction indicates that GDY may be an ideal material for interfacial modification on MOs. On this basis, the nanostructured $NiCo_2O_4$, TiO_2, CoO_x, MnO_2, IrO_2 and MoO_3 connected with GDY have been successfully prepared for various potential applications.[35–39] Therefore, it is of great significance to explore the synthesis of high quality GDY and GDY-based materials and reveal the relationship between their structures and properties. Here, this review systemically gives a summary and discussion of the synthesis methods of GDY/MOs.

2.2.1 Hydrothermal method. The hydrothermal method is an effective method for metal oxide synthesis, which utilizes a high-pressure, high-temperature water environment for chemical reactions. Under such conditions, the surface tension of water is reduced, the ion diffusion rate is accelerated, and the force between reactants is enhanced, which can promote crystallization and nucleation between reactants for the purpose of synthesizing the desired materials. A wide variety of materials can be synthesized by hydrothermal methods, and different products can be obtained according to different reaction conditions and reactant species. Typically, GDY/MOs were fabricated *via* a two-step process.[22] The first step was fabrication of GDY *via* a Glaser–Hay cross-coupling reaction. The second step was the synthesis of MOs on the

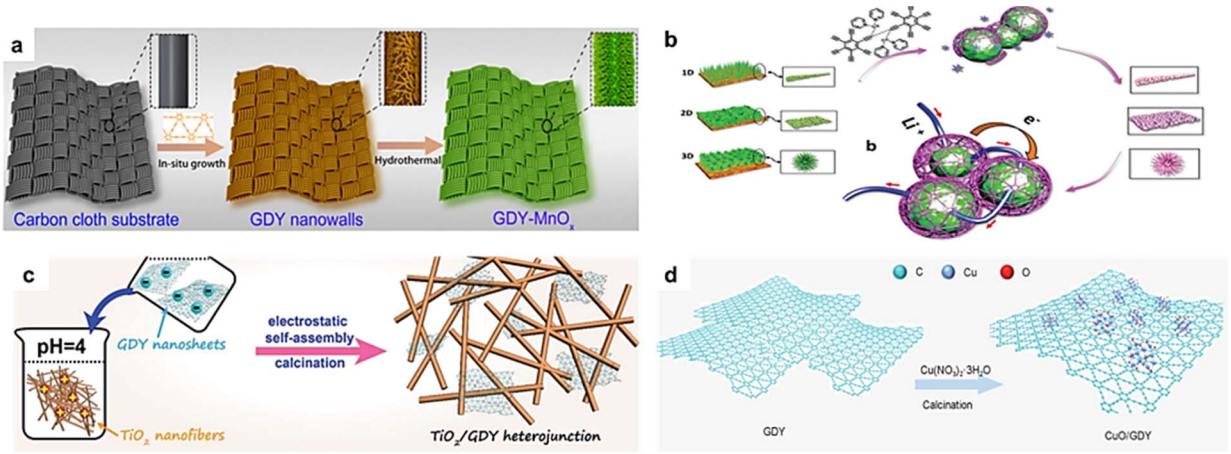

Fig. 2 (a) Synthesis of GDY/MnO_x;[38] (b) *in situ* construction of the multifunctional GDY on MOs with different dimensions;[41] (c) schematic diagram for the preparation of the TiO_2/GDY heterojunction;[3] (d) synthetic process of CuO/GDY.[25]

GDY by a modified hydrothermal method with the corresponding precursor. For instance, Fig. 2a shows the *in situ* preparation process of the GDY–MnO_x on a carbon cloth substrate.[38] Firstly, the GDY nanosheet was synthesized according to the previously reported Glaser–Hay coupling reaction.[40] Secondly, GDY–MnO_x was synthesized *via* a one-step hydrothermal method. A piece of as-synthesized GDY was added into 40 mL of 0.1 M neutral $KMnO_4$ aqueous solution in a Teflon-lined stainless-steel autoclave, which was kept at 160 °C for 24 h in an oven and then cooled to room temperature. After discarding the supernatant, the obtained nanocomposites were cleaned using distilled water several times to remove the remaining reactants and dried in a vacuum oven at 60 °C for 12 h. The *in situ* growth of GDY–MnO_x ensured the strong combination between GDY–MnO_x and carbon cloth, demonstrating excellent activity and stability. Furthermore, as shown in Fig. 2b, Li *et al.* achieved the growth of GDY under ultra mild conditions *in situ* for coating MOs ($NiCo_2O_4$, TiO_2, Al_2O_3, Co_3O_4, ZnO, Fe_3O_4, MnO_2) of complex dimensions.[41] The nanostructured MOs loaded on Cu foil were immersed into a solution containing the precursor of HEB for *in situ* weaving GDY nanosheets under room temperature (25 °C). The mild conditions were highly acceptable for constructing *in situ* a protective and conductive all-carbon layer on the MOs. During the growth of GDY, the GDY was initiated by the bottom Cu foil, and extended along the interfacial feature of the MOs due to the mass diffusion in the voids. This construction method of GDY nanosheets well conformed with the morphologies of MOs even with much complex features.

2.2.2 Electrochemical method. The electrochemical method was also adopted in the synthesis of GDY/MOs due to its ease of operation, mild and easy-to-control reaction conditions, and the absence of additional pollutants. Li *et al.* synthesized GDY@CoO_xQDs through an *in situ* growth-deposition strategy using the typical three-electrode system at the room temperature.[37] The as-prepared GDY, saturated calomel electrode (SCE) and carbon rod were used as the working electrode, reference electrode and counter electrode, respectively. The as-prepared GDY was kept in a cobalt chloride aqueous solution (50 mM, 50 mL) at a constant voltage of −0.6 V (*versus* SCE) for 1200 s, followed by being treated by cyclic voltammetry (CV) in the range of −1.0 V to 0.5 V at 100 mV s^{-1} for 200 segments. The obtained samples were washed carefully with deionized water under an Ar atmosphere and dried by an Ar flow. In addition, Yu *et al.* designed GDY coupled TiO_2 nanofibers by an electrostatic self-assembly approach.[36] The dispersed TiO_2 in water (pH = 4) was positively charged with a zeta potential of +15.1 mV, and GDY was negatively charged with a zeta potential of −19.2 mV. As schematically illustrated in Fig. 2c, the hybrid structure between TiO_2 and GDY was formed through the electrostatic self-assembly process.

2.2.3 Impregnation method. Impregnation method is a relatively simple but effective preparation method for GDY/MOs. The impregnation method can realize the precise control of the morphology, size and distribution of catalyst particles by adjusting the parameters such as the concentration of catalyst precursor, impregnation time and temperature. Therefore, the catalyst prepared by the impregnation method has good controllability of morphology and performance. Our group recently synthesized a sub-nanocluster CuO/GDY catalyst on a large scale with gram productivity using the impregnation method (Fig. 2d).[29] First of all, the designed HEB monomer was used through an *in situ* cross-coupling reaction on copper foil to fabricate GDY powder. Secondly, the GDY powder was ultrasonically removed from copper foil and then put into a $Cu(NO_3)_2 \cdot 3H_2O$/ammonia solution to sufficiently deposit Cu^{2+} ions on the GDY surface. The mixture solution was then stirred vigorously for 2–3 hours and dried at 50 °C overnight until the solvent ammonia was removed. Thirdly, the mixture was calcined at 400 °C under an argon atmosphere. Finally, the sub-nanocluster CuO was formed *in situ* on GDY. Moreover, we have successfully prepared different sizes of CuO nanoparticles on GDY through this method.[25] The catalyst can effectively activate molecular oxygen and further promote the removal of different kinds of pollutants.

2.3 The advanced characterization of GDY/MOs

The structure of GDY/MOs plays a decisive role in catalytic performance. It can affect the quality of the GDY/MO surface and the rate of chemical reaction, change the position of active centers, binding energy, structure, electron distribution and charge transfer, and other properties. Therefore, appropriate structural characterization methods for GDY/MOs are essential. The reported characterization methods of GDY/MOs mainly involve two categories: image and spectroscopy. The characterization methods of images include scanning electron microscopy (SEM), transmission electron microscopy (TEM), atomic force microscopy (AFM), and scanning transmission electron microscopy (STEM). The spectroscopy characterization contains Raman spectroscopy, X-ray photoelectron spectroscopy (XPS), X-ray absorption spectroscopy (XAS) and so on. The image characterization is mainly used to describe the morphology characteristics of the GDY/MOs (particle size, elemental distribution, crystal structure, phase composition, structural defects, grain boundary structure and composition, *etc.*). Spectroscopy characterizes the structure of the catalyst (chemical composition, compositional changes, molecular valence, electronic configuration, interfacial interaction).

2.3.1 Image based characterization techniques

2.3.1.1 SEM. SEM can be used to directly observe the surface structure of GDY/MOs, particle size, distribution, uniformity and agglomeration.

Combining with the energy spectrum, it can also be used to analyze their composition. For instance, Fig. 3a–c show the top SEM views of SnO_x/GDY nanowalls.[42] The top view demonstrated that vertical GDY nanowalls were *in situ* grown on the surface of the carbon cloth. The SEM images of GDY/MOs clearly describe the morphologies of GDY nanomaterials, including the height of the nanowalls, the size of nanoparticles and so on.

2.3.1.2 TEM. TEM and its associated electron diffraction, energy dispersive X-ray spectroscopy (EDX) and electron energy loss spectroscopy (EELS) are some of the most powerful methods for characterizing the morphology, crystal structure, composition and interfacial interaction of GDY/MOs. As shown in Fig. 3d–f,[37] TEM and HRTEM images showed that Co quantum dots (CoO_xQDs) were uniformly dispersed on the surface of porous GDY with the size of 3.7 nm. The CoO_xQDs were grown on GDY nanowalls in the form of nanoparticles and the interfacial interaction may be present between GDY and CoO_xOD. TEM is a commonly used method for characterizing GDY/MO morphology. However, this method is the result of local observation, so there are certain contingencies and statistical errors. The typical measurement range of TEM is 5 nm–500 μm. It is necessary to obtain the average particle size of nanoparticles through statistical analysis and measurement of particle size with a certain number of photos.

2.3.1.3 STEM. STEM has the advantages of high resolution and sensitivity to chemical composition, and provides better visual images of GDY/MOs compared with TEM. Very recently, our group demonstrated that the neighboring sp-hybridized C and Cu sites on the interface of the sub-nanocluster CuO/GDY

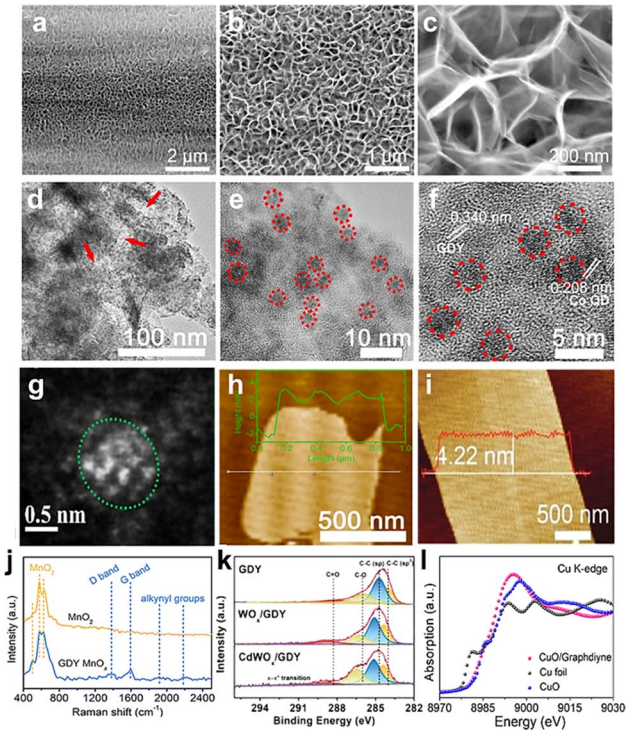

Fig. 3 (a–c) SEM images of SnO_x/GDY;[42] (d and e) TEM images of GDY@CoO_xQDs;[37] (f) HRTEM image of GDY@CoO_xQDs;[37] (g) STEM images of GDY/CuO;[29] (h) AFM images of GDY@CoO_xQDs;[37] (i) AFM image of IrO_x/GDY;[39] (j) Raman spectra of GDY/MnO_x and MnO;[38] (k) XPS spectra of WO_3, WO_x/GDY, and $CdWO_x$/GDY;[24] (l) XANES of CuO/GDY, CuO, and Cu foil.[29]

was the key structure to effectively modulate the O_2 activation process in the bridging adsorption mode.[29] The HAADF-STEM image (Fig. 3g) demonstrated the dark GDY and the relatively bright sub-nanocluster CuO. The particle size distribution of sub-nanocluster CuO from the HAADF-STEM image showed that the average particle size was around 0.82 nm. According to the HAADF-STEM image, the reconstruction model of the sub-nanocluster CuO suggested that the subnanocluster CuO was composed of 14 Cu atoms and 12 O atoms and there was interfacial chemical interaction between CuO and GDY. As an indispensable tool for in-depth study of GDY/MOs, STEM equipped with an aberration correction device can perform more precise and accurate structural characterization of GDY/MOs. With the introduction of the spherical error corrector, STEM with many analytical components can significantly improve the resolution to angstroms, and the ultra-high resolution can even clearly reveal the fine structure at the molecular level and atomic scale.

2.3.1.4 AFM. The AFM is capable of imaging samples in air or liquid and measuring the surface roughness and thickness of ultrathin 2D/quasi-2D GDY/MOs with high accuracy. As shown in Fig. 3h, the AFM images revealed that the GDY@CoO_xQD nanosheet had thickness around 4.0 nm.[37] Li *et al.* reported IrO_x quantum dots synthesized by GDY-induced *in situ* controllable growth to enhance their activity in acidic electrolytes. The AFM images of IrO_x/GDY showed a rough surface with numerous

individual bright dots protruding (Fig. 3i),[39] which implied the presence of QDs. In short, this characterization method is usually used to measure 3D surface topography and roughness of powder/film/bulk/fiber samples, nanosheet thickness, interphase thickness and so on. However, the use of AFM to characterize the interface structure of GDY/MOs is still rare.

2.3.2 Spectral based characterization techniques

2.3.2.1 Raman spectroscopy. Raman spectroscopy is an analytical method with scattering spectra to obtain information on molecular vibrations and rotations used for the structural characterization of GDY/MOs. In general, it can mainly be used to check the defects and bonding states of GDY. Fig. 3j shows the Raman spectra of MnO_2 and GDY/MnO_x. Compared with MnO_2, the newly appeared peaks at 1382, 1589, 1912 and 2187 cm^{-1} corresponded to the D band, G band and alkynyl groups for GDY, respectively, which confirmed the successful synthesis of GDY/MnO_x.[38] After the GDY was connected with MnO_x, the obvious shift of the G band and conjugated diyne link modes towards higher wave numbers can be observed, indicating the strong chemical interaction (charge transfer or chemical bonding) between GDY and metal species. Besides, MnO_x/GDY showed a larger I_D/I_G ratio than pure GDY, which indicated the increase of the defect sites after the combination of GDY and MnO_x. These results brought by the interactions between GDY and MnO_x are all beneficial to the enhancement of the catalytic activity. In summary, Raman spectroscopy is very sensitive to molecular bonding and the structure of the sample, so each molecule or sample will have its own unique spectral "fingerprints". These "fingerprints" can be used for chemical identification, morphology and phase, internal pressure/stress, and composition analysis. For GDY/MOs, Raman spectroscopy can not only show the unique alkynyl groups for GDY, but also supply some special structures of one kind of certain metal oxides.

2.3.2.2 XPS. XPS was mainly employed to check the existence of elements and measure the relative contents of GDY/MOs within the escape depths of photoelectrons in the near surface regions. Generally, information such as elemental composition, chemical state and molecular structure on the surface of the GDY/MOs can be obtained from the peak position and peak shape of the XPS. The content or concentration of the element on the surface of the samples can be obtained from the peak strength. Moreover, XPS can be used for verifying the interactions between GDY and MOs. As shown in Fig. 3k,[24] the C 1s XPS spectra showed the characteristic peaks of sp-C, sp^2-C, C–O, and C=O for GDY, WO_x/GDY, and $CdWO_x$/GDY samples, demonstrating the robustness of GDY structures. Additionally, the sp-C for both WO_x/GDY and $CdWO_x$/GDY shifted to higher binding energies than that of GDY, implying the electron loss from sp-C to metal species. Compared with GDY, the newly appeared π–π* transition peak verified the interactions between GDY and WO_x or $CdWO_x$. Besides, the XPS results showed only the presence of W^{6+} in WO_3, while the W 4f spectra of WO_x/GDY and $CdWO_x$/GDY all can be deconvoluted into two doublets corresponding to W^{6+} (35.8 eV for W $4f_{7/2}$ and 37.9 eV for W $4f_{5/2}$) and W^{5+} (35.3 eV for W $4f_{7/2}$ and 37.4 eV for W $4f_{5/2}$). These results indicated the presence of mixed-valent W species due to the charge transfer from sp-C in GDY to metal atoms. Therefore, XPS is a commonly used analytical technique to characterize the surface/interface composition of GDY/MOs, which is important for the investigation of the structure–performance relationship.

2.3.2.3 XAS. XAS is generally used to reflect the valence state of a single element, the coordination environment and the electronic structure of a single absorbing atom in GDY/MOs. For instance, Fig. 3l shows the X-ray absorption near edge structure (XANES) spectra at the Cu K-edge of the CuO/GDY catalysts, CuO, and Cu foil.[29] Compared with Cu foil, the absorption edge of CuO/GDY shifted to a higher energy, close to that of CuO, indicating that the valence state of Cu in CuO/GDY was approximately +2. Besides, the results also indicated that there may be interfacial chemical bonds between CuO and GDY. In combination with XPS and Raman spectra, the structure and the interactions between GDY and MOs can be more accurately characterized.

3 Critical molecule activation behavior on GDY/MOs for efficient energy and environmental catalysis

In order to achieve efficient energy and environmental catalysis of GDY/MOs, the investigation of relevant reaction mechanisms is essential. Notably, the effective activation of important reactant molecules is the critical step towards efficient catalysis.[43] Reactant molecules such as water (H_2O), oxygen (O_2), and nitrogen (N_2) are important participants in environmental energy catalytic reactions, and their effective activation contributes to the improvement of GDY/MOs' catalytic performance.[44,45] In the following, we will discuss in detail the activation behavior of these critical reactant molecules based on the GDY/MOs in the field of energy and environmental catalysis.

3.1 Activation of H_2O

H_2O, as one of the most important compounds on the earth, widely exists in nature and plays an important role in heterogeneous catalytic chemical reactions. In the field of energy conversion, H_2O is a clean reactant that can be activated and dissociated to generate hydrogen and oxygen, and other products.[42,46] In the field of environmental remediation, H_2O can act as an effective promoter or co-catalyst to enhance catalytic activity.[43,47] GDY/MOs with a highly tunable interface structure due to the unique diacetylene bonds (–C≡C–C≡C–) in GDY can provide more adsorption sites for H_2O compared to other catalysts for H_2O activation. The activation and dissociation of H_2O molecule over GDY/MOs mainly produce hydrogen and hydroxyl species, which are the key species involved in catalytic reactions in the field of energy conversion and environmental remediation. There are two main mechanisms of H_2O activation into reactive species (Fig. 4):[48,49] one is the homolysis of water to produce hydroxyl radicals and hydrogen radicals; the other is the production of hydrogen protons and hydroxyl species by electrostatic forces or van der Waals forces.

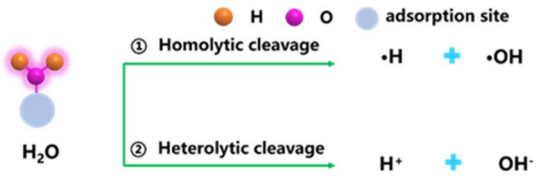

Fig. 4 Two main mechanisms of H_2O activation.

3.1.1 Hydrogen species. The hydrogen species generated through the activation and dissociation of H_2O in chemical reactions are commonly used as a source of hydrogen or a reducing agent, participating in the reaction.[45,50] There have been many studies on the interface structure design of GDY/MOs to activate H_2O and generate H species for efficient energy and environmental catalysis. For example, our group reported an original three-dimensional self-supporting graphdiyne/molybdenum oxide (GDY/MoO_3) material for an efficient HER *via* a rational design of "sp C–O–Mo hybridization" on the interface.[22] As shown in Fig. 5a, the "sp C–O–Mo hybridization" facilitated charge transfer and boosted the activation of H_2O molecules, as well as the adsorption and combination of the generated hydrogen species to form H_2 molecules. A rationally designed interfacial structure enables water activation to produce hydrogen species more easily, achieving excellent HER performance, which will be discussed in the following sections. In addition, coupling hydrogen species produced by water activation and optimization of the key intermediate adsorption is an important way toward a high-efficiency CO_2RR. For example, Li *et al.* found that GDY has advantages in effectively regulating the valence state of SnO_x. The operando *in situ* infrared measurement and DFT calculation results revealed that the limiting potential was determined by the step of OCHO* hydrogenation (Fig. 5b). The effective water activation to produce hydrogen species is the key to OCHO* hydrogenation. Moreover, GDY/SnO_x can selectively and efficiently generate and stabilize the key *OCHO intermediates and promote the formation of formate by completely inhibiting the competing HER, promoting the CO_2RR.

3.1.2 Hydroxyl species. The hydroxyl species, also produced by water activation and dissociation, play a crucial role in many catalytic reactions related to energy and environment. However, different from the hydrogen species, hydroxyl species are mainly involved in oxidation reactions, which serve as the key intermediate species or oxidizing agent. Hydroxyl species mainly include the hydroxyl functional groups (*OH) adsorbed on the surface of the catalyst and the hydroxyl radicals (˙OH). For example, the generation of hydroxyl functional groups through water activation is the first step in the mechanism of the OER. Li's group verified that the lower valence of Ir atom ($<4^+$) induced by the strong electronic interaction with GDY was more favorable for the adsorption and desorption of active intermediates (*i.e.*, OH*, O*, OOH*),[39] effectively promoting the progress of the OER (Fig. 5c and d). Additionally, water

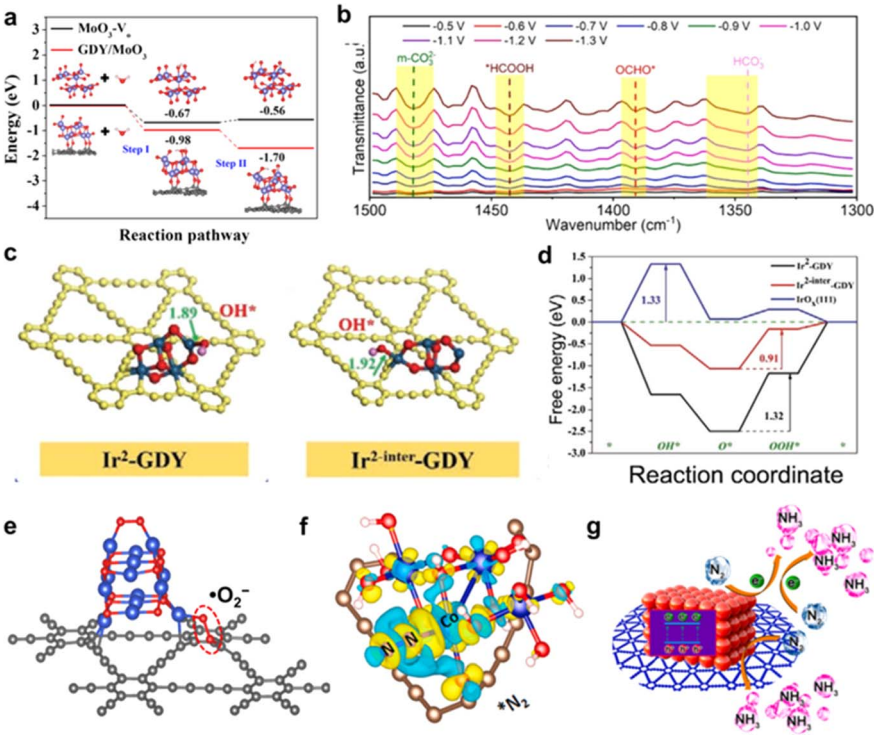

Fig. 5 (a) Calculated energy diagram of H_2O adsorption and H_2O dissociation (inset: corresponding atomic structures of the initial state, H_2O adsorption and water dissociation on MoO_3-V_o and GDY/MoO_3);[22] (b) the operando *in situ* infrared spectra of SnO_x/GDY at different potentials;[31] (c) optimized adsorption structures of OH* on Ir^2-GDY site and $Ir^{2\text{-inter}}$ site, respectively;[39] (d) free energy diagrams of the OER on the Ir sites at equilibrium potential;[39] (e) configuration of the O_2 molecule adsorbed on the interface of CuO/GDY;[29] (f) differential charge density distributions of (e) $*N_2$ adsorbed on CoO_xQDs/GDY;[37] (g) schematic diagram of the ammonia production process on porous GDY@CoO_xQDs.[37]

activation has also demonstrated its role in the field of air pollutant control. For example, our group recently reported that the MoO_3/GDY catalyst facilitated the activation of water to hydroxyl species, promoting the decomposition of O_3. The sp-C in diacetylene bonds of GDY can donate electrons to MoO_3 through the C–O–Mo bond, which effectively promoted water molecule adsorption on Mo sites of MoO_3/GDY, and readily dissociate to H* and OH* intermediates. The adsorption energy of O_3 on MoO_3/GDY-2OH (hydroxyl site, −1.19 eV) was much lower than on MoO_3/GDY (−0.1 eV), which indicated that the hydroxyls dissociated from the adsorbed water on MoO_3/GDY were the adsorption sites under humidity conditions, facilitating rapid and efficient O_3 decomposition under high humidity.[8]

3.2 Activation of O_2

Oxygen (O_2) is an important gas that plays an indispensable role in oxidation reactions or generating chemical energy. However, the spin triplet state of oxygen is very stable and finds it difficult to directly participate in the chemical reaction. So, the issue of how to convert oxygen into reactive oxygen species (ROS, $\cdot O_2^-$, O_2^{2-}, $\cdot OH$, O_2^1, *et al.*) through chemical processes under mild conditions is still facing serious challenges. There are two main mechanisms of O_2 activation into ROS (Fig. 6):[29,51–54] energy transfer mechanism and electron transfer mechanism. In the energy transfer mechanism, the spin electron state of the spin-triplet state ($^3\sum$) O_2 molecule is changed to $^1O_2$ *via* physical, chemical and biological methods. The electron transfer mechanism occurs through a continuous single-electron reduction process to sequentially form $\cdot O_2^-$, O_2^{2-}, and $\cdot OH$.

The rapid activation of oxygen at the active site of the GDY/MOs to produce ROS is considered to be the main reaction pathway for degradation of antibacterial and aqueous/gaseous pollutants. However, there are few studies on the activation of oxygen by GDY/MOs. Zhang's group found that the generation ability of ROS ($\cdot O_2^-$, $\cdot OH$, O_2^1) and H_2O_2 was significantly enhanced after TiO_2 nanofibers were incorporated into GDY.[36] Hence TiO_2/GDY showed superior photocatalytic antibacterial activities compared to TiO_2. Moreover, oxygen activation plays an important role in the thermocatalytic degradation of gaseous pollutants. Recently, our group reported that the neighboring sp-hybridized C and Cu sites on sub-nanocluster CuO/GDY can effectively activate O_2 to $\cdot O_2^-$ in the bridging adsorption mode for CO oxidation (Fig. 5e).[29] The unique sp-hybridized carbon in GDY could promote the activation of molecular oxygen to produce more ROS compared with the sp^2-hybridized carbon in graphene, achieving excellent CO oxidation performance. In brief, GDY/MOs possess strong ability towards oxygen activation due to the interaction between GDY and MOs. And more GDY/MOs deserve to be designed and developed for energy and environmental applications.

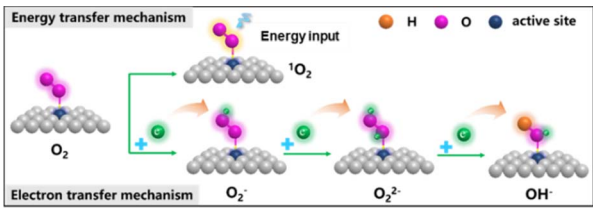

Fig. 6 Two main mechanisms of O_2 activation.

3.3 Activation of N_2

N_2 activation at ambient temperature and pressure is a great challenge. Researchers have made great efforts to this end. The first step of N_2 activation is the adsorption of N_2 at the active site. Owing to the unique electronic structure of GDY, the efficient electron transfer between GDY and MOs in GDY/MOs can boost the adsorption/desorption of N_2 and intermediate species. For example, GDY-induced iron vacancies in the ferroferric oxide/graphdiyne heterostructure (IVR-FO/GDY) promoted the generation of Fe vacancies in the crystalline structure and regulated the Fe valence state. The formation of iron vacancies activated the local O sites to transfer electron towards GDY, leading to GDY preserving the electron-rich feature, which facilitated electron transfer towards adsorbates. Thus, the N_2 molecule was efficiently activated and could readily form *NNH. Moreover, IVR-FO/GDY with the iron vacancies promoted the transformation of key intermediate species (*e.g.*, from $*NH_2NH$ to $*NH_2NH$), resulting in impressive electrocatalytic nitrogen fixation ammonia performance. In addition, Li's group found that electrons could be transferred from the Co site to the π* orbital of N_2 on GDY based quantum dots (GDY@CoO_xQDs), which effectively weakened the N≡N bond facilitating the effective activation of N≡N bonds and the formation of the Co–N bond (Fig. 5f and g). CoO_xQDs/GDY exhibited superior N_2 adsorption and N_2 activation abilities, leading to excellent photocatalytic performance for ammonia synthesis.[37]

4. Applications of GDY/MOs in catalysis

Based on the above discussion on the activation of reactant molecules by GDY/MOs, it can be seen that the interfacial interactions between GDY and MOs can effectively modulate the morphological and electronic structures of MOs, promoting the activation of reactant molecules (*e.g.*, H_2O, O_2, N_2, *etc.*) and regulating the adsorption of intermediate species, and thus the intrinsic activity of the catalyst was significantly enhanced. Besides, GDY is an emerging carbon material with a unique two-dimensional layered conjugated system, natural intrinsic band gap and ultra-high carrier mobility.[9,55–60] Combining it with MOs can promote charge transfer and ion diffusion, and improve electrochemical reactivity and kinetics, which shows great performance advantages and application prospects in the fields of energy and environmental catalysis.

4.1 Applications of GDY/MOs in energy catalysis

GDY/MOs demonstrate promising applications in energy catalysis, such as the hydrogen evolution reaction (HER),[22]

oxygen evolution reaction (OER),[61] nitrogen reduction (NRR),[62] and battery energy storage.[63]

4.1.1 Hydrogen evolution reaction. Hydrogen energy, as a secondary energy source with abundant sources, and a widely used green and low-carbon fuel, is an important carrier to achieve green transition of energy.[64–67] Hydrogen production by electrochemical water splitting is an efficient and clean hydrogen production technology, with a simple hydrogen production process and high product purity, which is one of the most promising technologies for large-scale hydrogen production. There have been many articles about GDY/MOs used for HER applications. Li's group reported that GDY-coated nickel oxide heterostructures (NiO-GDY) effectively facilitated charge transfer (Fig. 7a), which promoted the activation of H_2O molecule and the generation of hydrogen species, thereby achieving superior HER performance to that of Pt/C (η_{10} mA cm^{-2} = 58 mV *versus* 85 mV) (Fig. 7b and c).[68] The unique advantages of GDY enable the facile and controllable fabrication of the ideal interfacial structure with high activity. Based on this, Li's group also prepared a hierarchical three-dimensional (3D) heterostructure of GDY@$NiO_x(OH)_y$ for the HER in 1 M KOH.[69] The strong interactions between GDY and $NiO_x(OH)_y$ greatly enhanced charge transfer ability and accelerated reaction kinetics, as well as the largest electrochemical active surface area. The activity of GDY@$NiO_x(OH)_y$ can be maintained after continuous electrolysis for 190 h at 20 mA cm^2 (η = 331.7 mV), which was much better than that of GDY and $Ni(OH)_2$. Iron/cobalt layered double-hydroxide nanosheet arrays (e-ICLDH@GDY) were also investigated by Li's group.[70] The stable adsorbed H bonds with the C site on GDY, and the H_2O molecule adsorbs onto Fe sites on the ICLDH, which is beneficial for the two closely adsorbed H atoms to combine, resulting in potentially efficient H_2 generation. Recently, Li's group constructed a two-layer heterojunction with an sp-hybrid carbon–oxygen–rhodium (sp-C–O–Rh) double-layer sandwich interface in GDY/RhO_x/GDY.[72] GDY/RhO_x/GDY exhibited improved performance in alkaline-simulated seawater, with a much smaller overpotential of 9 mV at 10 mA cm^{-2} and a smaller Tafel slope (42 mV dec^{-1}) than the pure GDY (550 mV@η_{10}, 479 mV dec^{-1}), commercial 20 wt% Pt/C (71 mV@η_{10}, 48 mV dec^{-1}), and RhO_x (35 mV@η_{10}, 55 mV dec^{-1}). The formation of sp-C–O–Rh bonds between GDY and RhO_x enhanced the charge transfer ability from RhO_x to GDY, resulting in a more electron-rich surface and increased active sites. Moreover, sp-C–O–Rh bonds may lead to moderate H_2O dissociation and H* adsorption energies. The adsorption/desorption energies for reaction intermediates were significantly optimized, resulting in a substantial enhancement in electrocatalytic performance for

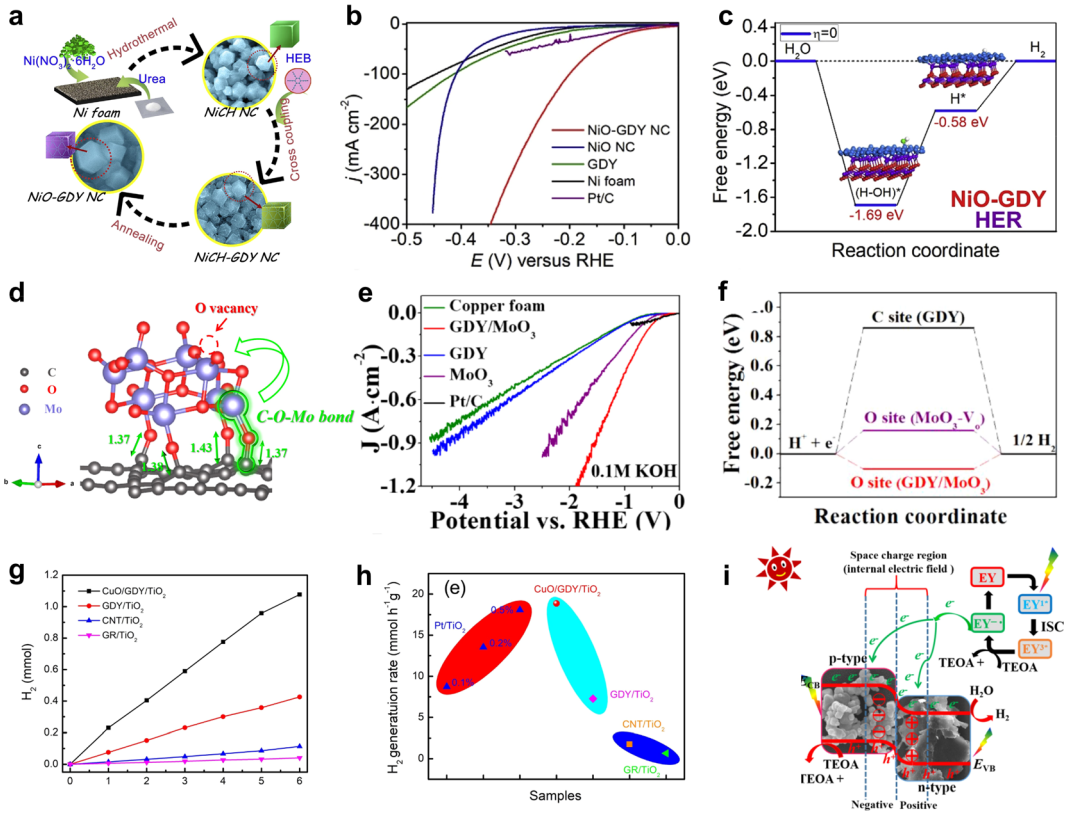

Fig. 7 (a) The synthetic strategy for NiO-GDY;[1] (b) polarization curves of NiO-GDY, NiO, GDY, Ni foam and Pt/C for the HER in 1.0 M KOH;[1] (c) energy diagram for the HER on NiO-GDY;[68] (d) C–O–Mo bonds at the interface between MoO_3 and GDY;[22] (e) polarization curves of the samples with high-current density in 0.1 M KOH;[22] (f) the free energy of hydrogen adsorption (ΔG_{H*}) on GDY, MoO_3-V_o and GDY/MoO_3;[22] (g) H_2 evolution of CuO/GDY/TiO_2, CNT/TiO_2 and GR/TiO_2;[71] (h) comparison of the H_2 generation rate based on different photocatalysts;[71] (i) photocatalytic hydrogen evolution mechanism of GO-15.[21]

the HER in alkaline-simulated seawater. Our group reported GDY/MoO_3 with the sp C–O–Mo hybridization on the interface (Fig. 7d).[22] As shown in Fig. 7e and f, the ΔG_{H^*} value of GDY/MoO_3 is −0.11 eV, which is a preferable value for both hydrogen adsorption and desorption than GDY and MoO_3, achieving a high-current density HER (>1.2 A cm^{-2}) in an alkaline electrolyte and a decent activity and stability in natural seawater. The "sp C–O–Mo hybridization" facilitated charge transfer and boosted the dissociation of H_2O molecules, as well as the adsorption and combination of the generated hydrogen species to form H_2 molecules.

GDY/MOs not only demonstrate excellent performance in electrochemical hydrogen evolution but also exhibit remarkable potential in photocatalytic hydrogen evolution.[73] For example, CuO/GDY as a cocatalyst effectively promoted photogenerated carrier separation in TiO_2 owing to the solid junction between GDY and CuO,[71] facilitating the combination of hydrogen protons dissociated from water with electrons to produce hydrogen. Jin *et al.* reported a Co_3O_4/GDY catalyst (GO-15) with the p–n heterojunction, exhibiting a strong hydrogen evolution activity (2336.6 μmol g^{-1} h^{-1}), which is 8.6 and 3.8 times higher than that of GDY and Co_3O_4.[21] The coexistence of Co^{2+}/Co^{3+} and a strong internal electric field in GO-15 greatly promoted charge separation and diversion of photon-generated carriers and accelerated the adsorption of eosin Y and hydrogen ions, which exhibited excellent photocatalytic H_2 production performance.

4.1.2 Oxygen evolution reaction. Water splitting is a sustainable way of producing H_2 from clean fuels, represented by the HER and OER. However, the OER remains a bottleneck due to its sluggish kinetic process, which dominates the efficiency of overall water splitting.[74] The OER mechanism involves the adsorption and desorption of intermediate species, including the $OH_{ads} \rightarrow O_{ads} \rightarrow OOH_{ads} \rightarrow O_{2ads}$ process. The generation of hydroxyl functional groups through water activation is the first step in the mechanism of the OER. The naturally distributed cavity structures and abundance of sp-carbon atoms in GDY endow it a strong affinity for metal atoms or metal oxides.[57] This unique structure promotes the controlled growth of GDY nanostructures, which enables the catalyst to possess suitable adsorption and desorption capabilities towards intermediate species, resulting in highly active and durable catalytic performance.[55,75] Li's group reported the IrO_xQDs/GDY catalyst with a current density of 10 mA cm^{-2} at a small overpotential of 236 mV and a Tafel slope of 70 mV dec^{-1}, exhibiting excellent

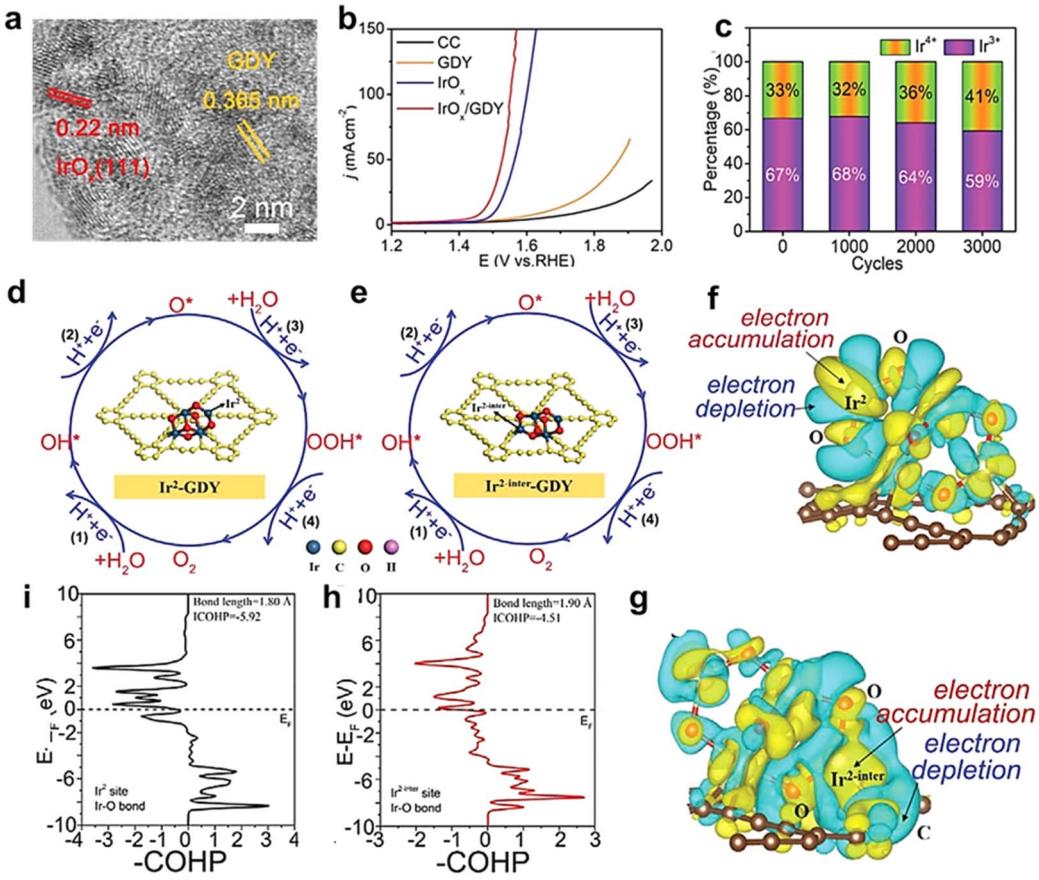

Fig. 8 (a) High-resolution TEM images of IrO_xQDs/GDY; (b) polarization curves of IrO_xQDs/GDY, IrO_x, GDY, and CC for the OER in 0.5 m H_2SO_4 at a scan rate of 2 mV s^{-1}; (c) the percentage of Ir^{3+} and Ir^{4+} species in the catalyst after different cycles; four consecutive elementary electron steps on (d) non-heterogeneous and (e) heterogeneous interfacial iridium sites, respectively; differential charge density distribution of (f) non-heterogeneous interfacial iridium atom and (g) heterogeneous interfacial iridium atom, respectively; crystal orbital Hamilton populations (COHPs) of (i) Ir^2 site (black line) and (h) $Ir^{2\text{-inter}}$ site.[39]

activity and durability for acidic OER (Fig. 8a and b).[39] For Ir (Fig. 8c), the percentage of Ir^{4+} increased from 33% to 36% and 41% after 2000 CV and 3000 CV, respectively, demonstrating that the relative contents of the Ir^{3+} and Ir^{4+} could rationally modulate the catalytic performance. DFT calculations verified that the lower valence of Ir atom (<4$^+$) induced by the strong electronic interaction with GDY was more favorable for the adsorption and desorption of active intermediates (*i.e.*, OH*, O*, OOH*), effectively promoting the progress of the OER (Fig. 8d–i). In addition, Li's group also reported a nanowire-structured $MnCo_2O_4$/GDY heterojunction catalyst (NW-$MnCo_2O_4$/GDY) for both the OER and HER in alkaline electrolytes with high catalytic activity and stability (Fig. 9a–c).[61] The obvious charge transfer between $MnCo_2O_4$ and GDY at the interface sites adjacent to the acetylenic chains in $MnCo_2O_4$/GDY, can effectively catalyze the elemental steps of the water splitting (Fig. 9d and e). DFT calculations showed that the binding energy of H_2O molecule on NW-$MnCo_2O_4$/GDY (1.74 eV) was much larger than that on pure NW-$MnCo_2O_4$ (0.10 eV) (Fig. 9f), while the free energy on NW-$MnCo_2O_4$/GDY (*i.e.*, −0.53 eV) was much lower than that on NW-$MnCo_2O_4$ (*i.e.*, −1.36 eV) (Fig. 9g), implying that the NW-$MnCo_2O_4$/GDY favored the adsorption and splitting of H_2O. The electron-rich metal site on NW-$MnCo_2O_4$/GDY enhanced the electro-negativity of the OH* intermediate (Fig. 9h), thereby facilitating the desorption or oxidation of OH* to form O* and HOO* intermediates during the OER process. The adsorption and desorption of active intermediates have a significant effect on the performance of the OER. Xue *et al.* reported that NiO_x/GDY with mixed valence states showed a smaller overpotential of 310 mV at 10 mA cm^{-2} than $Ni(OH)_2$/GDY and NiOOH/GDY for the OER. The induction of GDY accelerated the charge transfer, thereby boosting the OER performance.[76] The above studies have also achieved outstanding results in GDY-based materials for the OER. However, more systematic studies on the influence of the structure of GDY/MOs on the adsorption and desorption of intermediate species is lacking. Besides, there is currently limited research on the detailed and in-depth mechanism of water oxidation (active sites, intermediates, rection pathway, *etc.*). Therefore, more and more comprehensive and straightforward theoretical work is still worth looking forward to, which will have more direct guiding significance for design of GDY/MOs with high activity and stability for the OER.

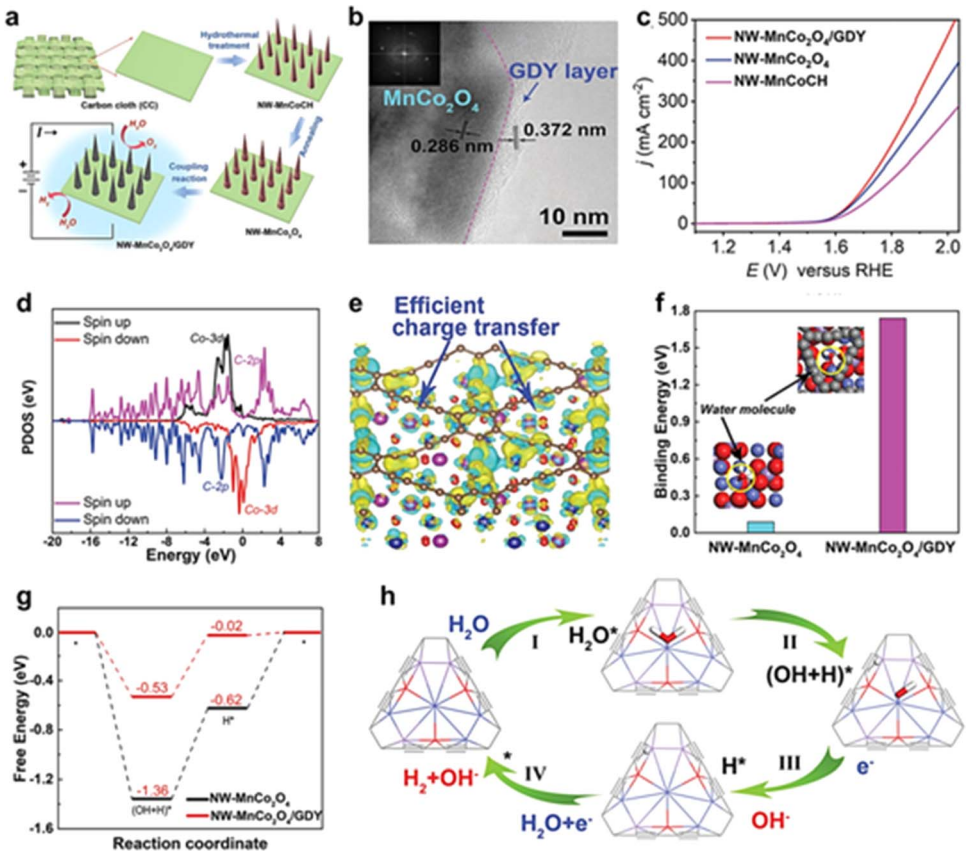

Fig. 9 (a) The synthesis routes for the catalysts; (b) HRTEM, and SAED images of NW-$MnCo_2O_4$/GDY; (c) polarization curves of NW-$MnCo_2O_4$/GDY, NW-$MnCo_2O_4$, and NW-MnCoCH for the OER with a scan rate of 2 mV s^{-1}; (d) the PDOS of Co and C atoms in the interface of NW-$MnCo_2O_4$/GDY; (e) the corresponding differential charge density distribution map of NW-$MnCo_2O_4$/GDY. Green and yellow areas represent the electron deletion and electron accumulation, respectively. The isosurface was set to 0.005 e bohr^{-3}; (f) the binding energy of water molecules adsorbed on NW-$MnCo_2O_4$ and NW-$MnCo_2O_4$/GDY, respectively. (g) The free energy of H_2O molecule dissociation and hydrogen evolution on NW-$MnCo_2O_4$ and NW-$MnCo_2O_4$/GDY, respectively; (h) schematic diagram of the proposed water splitting mechanism of NW-$MnCo_2O_4$/GDY.[61]

4.1.3 NH_3 synthesis. NH_3 is considered as a future fuel alternative and hydrogen storage molecule.[10,77,78] However, the NRR with high yield rates to meet industrial requirements is limited by the large kinetic barrier to break the stable N≡N triple bond (N≡N bonds up to 941 kJ mol^{-1}).[10] The Haber–Bosh reaction can efficiently convert nitrogen (N_2) to NH_3, but requires high temperature (300–500 °C) and pressure (150–200 atm), and is highly energy-consuming.[37] It would be ideal if N_2 conversion could be achieved at room temperature and atmospheric pressure. Electrocatalytic nitrogen fixation to ammonia (ENFA) has received widespread attention due to its advantages of low energy consumption, controllable reaction and green environmental protection. The efficient ENFA can efficiently convert the thermostable and chemical inert N_2 to NH_3 under ambient conditions.[78] It has been reported that GDY has incomparable superiority over traditional carbon materials in the electrocatalysis field due to the infinite natural pores, evenly distributed surface charges, and high conductivity. It can effectively combine and regulate the morphology and electron structure of metal species, generating new active sites, facilitating electron transfer, and achieving excellent electrocatalytic activity.[18,79,80] Huang and Li's groups utilized the advantageous properties of GDY in designing and fabricating an iron vacancy-rich ferroferric oxide/graphdiyne heterostructure (IVR-FO/GDY) for high-efficiency ENFA.[62] The GDY-induced iron vacancies in IVR-FO/GDY promoted the generation of Fe vacancies in the crystalline structure and regulated the Fe valence state (Fig. 10), which facilitated electron transfer and boosted the efficient activation and adsorption/desorption of N_2 and intermediate species. The ammonia yield (Y_{NH_3}) was up to 60.88% and faradaic efficiency (FE) was up to 60.88%, leading to excellent ENFA performance. Different from ENFA, photocatalysis nitrogen fixation to ammonia (PNFA) uses the sustainable sunlight to drive NH_3 synthesis from N_2 and H_2O at ambient temperature and pressure, which is a promising alternative for energy-consuming Haber–Bosh processes. The excellent hole transport properties of GDY endow GDY-based materials with natural advantages for photocatalysis.[81,82] Li's group prepared cubic-like GDY@Fe_3O_4 (GDY@Fe-A) and rod-like GDY@Fe_3O_4 (GDY@Fe-B) for PNFA(Fig. 11).[82] The coordination environment and valence states of Fe atoms were effectively regulated by GDY, which tuned the photocatalytic performance of the Fe_3O_4.[62] The significant charge transfer between GDY and Fe-B promoted the increase of the OV number for GDY@Fe-B. Thus, GDY@Fe-B could generate more electron hole pairs under illumination, and effectively suppress the recombination of the generated electron–hole pairs, leading to effective nitrogen activation and high photocatalytic performance. GDY@Fe-B showed remarkable catalytic performance with an unprecedented Y_{NH_3} level of 1762.35 ± 153.71 μmol h^{-1} g_{cat}^{-1} (the highest Y_{NH_3} could reach 1916.06 μmol h^{-1} g_{cat}^{-1}). The Li group also reported another high-performance graphdiyne/metal oxide hybrid material (GDY based quantum dots, GDY@CoO_xQDs) for NH_3 synthesis from N_2 and H_2O (Fig. 12).[37] The GDY with acetylenic bonds, natural pores and high reduction ability contributed to *in situ* decoration and stabilization of Co quantum dots. The introduction of GDY and the coexistence of Co^{2+}/Co^{3+} could facilitate electron transfer, which was beneficial for the adsorption and activation of N_2.

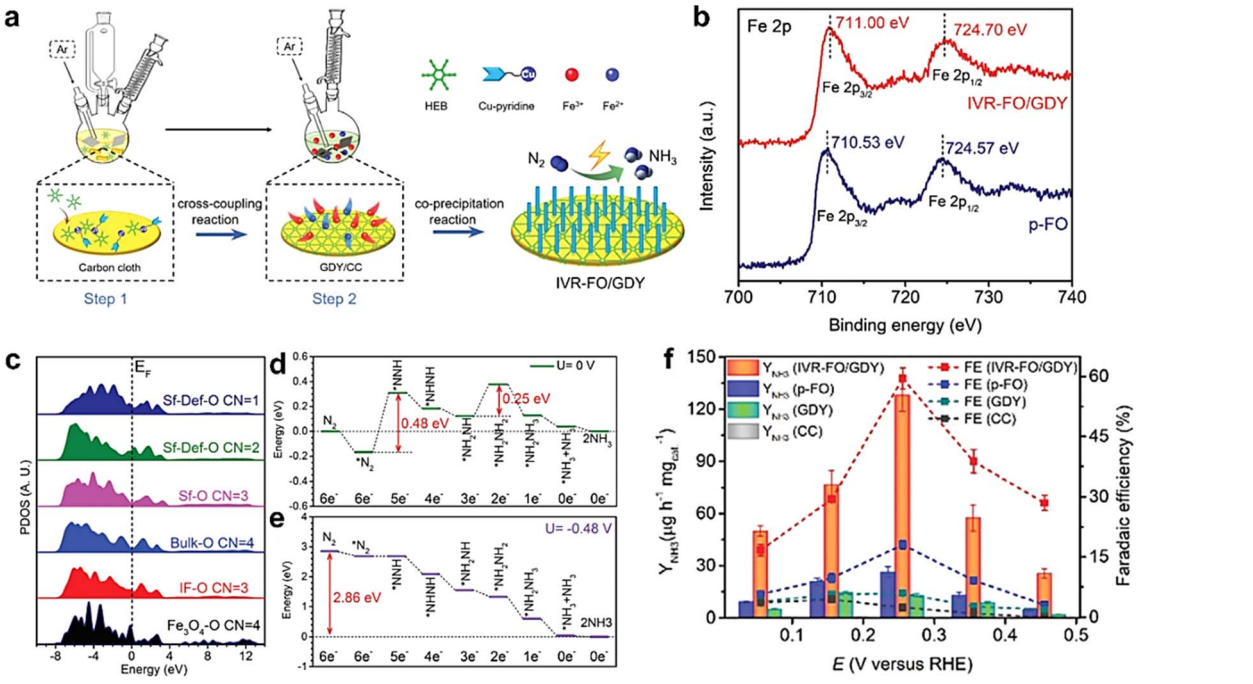

Fig. 10 (a) The synthesis route of the IVR-FO/GDY catalyst; (b) Fe 2p XPS spectra of IVR-FO/GDY and p-FO; (c) the site-to-site PDOS of O-2p orbitals in IVR-FO/GDY; (d) energetic pathway of the electrocatalytic NRR on IVR-FO/GDY under $U = 0$ V; (e) energetic pathway of the electrocatalytic NRR on IVR-FO/GDY under $U = -0.48$ V; (f) Y_{NH_3} and FEs of the samples at different potentials in N_2-saturated 0.1 m Na_2SO_4 (bars represent standard deviation).[62]

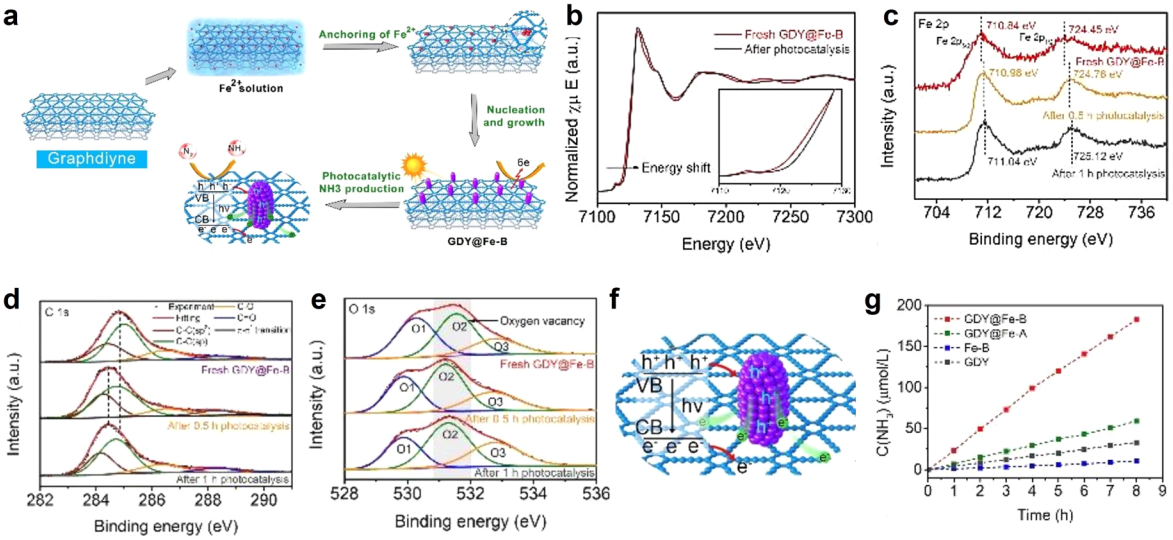

Fig. 11 (a) Schematic illustration of the synthetic and reaction routes for GDY@Fe-B; (b) XANES spectra of GDY@Fe-B at the Fe K-edge after photocatalysis; (c) Fe 2p; (d) C 1s and (e) O 1s XPS spectra of GDY@Fe-B along with photocatalysis time; (f) schematic illustration of the mechanism of the photochemical nitrogen reduction reaction on GDY@Fe-B; (g) ammonia concentrations as the function of time for the catalysts under irradiation.[82]

The electrons from the Co site were transferred to the π^* orbital of N_2 and formed a Co–N bond, leading to the enhancement of the PNFA performances. The Y_{NH_3} of GDY@CoO_xQDs could reach 26 502 μmol h^{-1} g_{cat}^{-1} in 46 repeated experiments, 100% selectivity, as well as a high long-term stability at room temperatures and pressures.

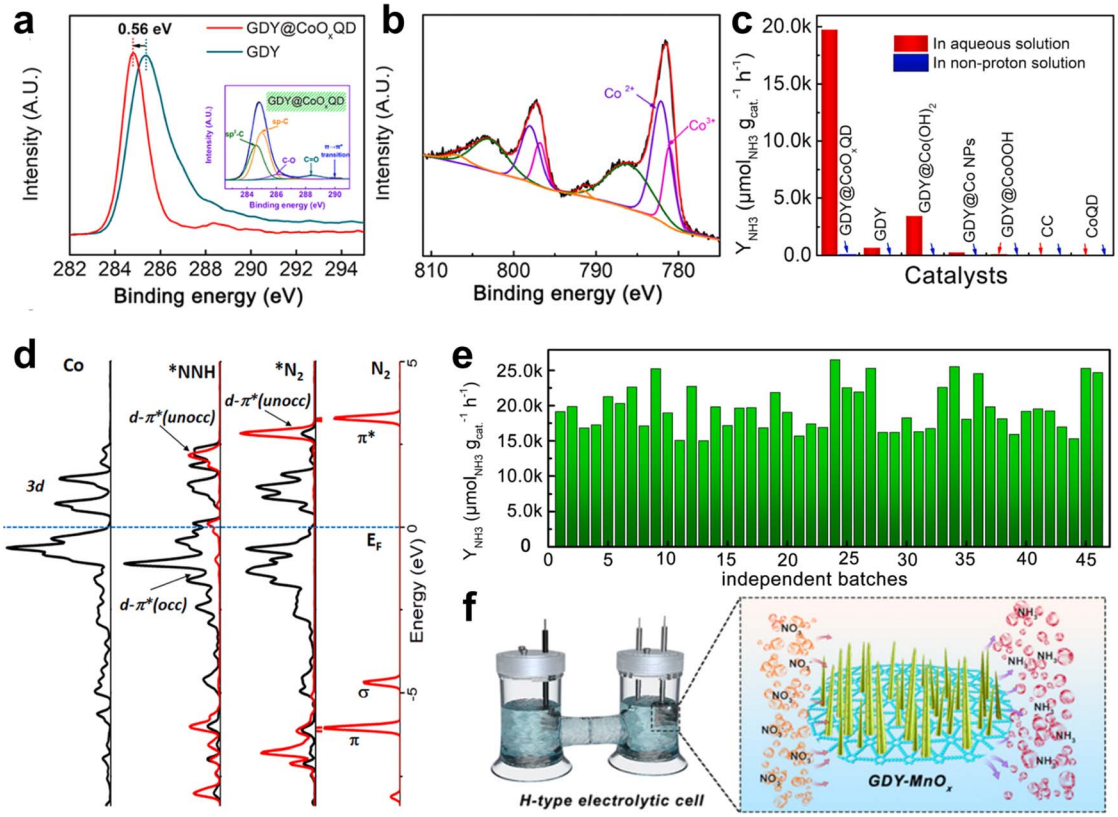

Fig. 12 (a) C 1s XPS spectra of GDY@CoO_xQDs and GDY. The inset is the deconvoluted C 1s XPS spectrum of GDY@CoO_xQDs; (b) the deconvoluted Co 2p XPS spectra of GDY@CoO_xQDs; (c) the NH_3 yield rates of the samples in different solutions; (d) the orbital distributions and the corresponding differential charge density distributions of $*N_2$ and *NNH adsorbed on CoO_xQDs/GDY; (e) Y_{NH_3} of the GDY@CoO_xQDs in independent experiments;[37] (f) illustration of the NO_3 to NH_3 conversion in an H-type electrolytic cell.[38]

Besides, the electrocatalytic nitrate reduction reaction (NtRR) has shown great potential for efficient NH_3 synthesis at room temperature and ambient pressure. Li's group reported the GDY–MnO_x heterointerface for highly selective and active NH_3 synthesis.[38] It is found that the incomplete charge-transfer between GDY and Mn atoms at the interface structures lead to the formation of new active sites, increasing the number of active sites. The electrocatalytic NtRR test results showed that the GDY–MnO_x exhibited excellent electrocatalytic performance for NH_3 synthesis with a large NH_3 yield of 463.4 μmol h^{-1} cm^{-2} and a high FE of 95.4% and long-term stability in 0.1 M KOH + 0.1 M NO_3^- aqueous electrolytes at room temperature and ambient pressure.

4.1.4 Battery energy storage. GDY/MOs are also widely used in the field of battery energy storage due to their unique electronic structure properties. The applications of GDY in battery energy storage were initiated by theoretical predictions. In 2012, the Searles group used DFT calculations to predict the 18-C hexagons of GDY (Fig. 13a) as a promising Li adsorption storage material; compared to 6-C hexagons (Fig. 13b), Li-atoms were captured by the 18-C hexagon with a maximum loading of LiC_3.[83] In 2013, Zhao *et al.* studied the Li diffusion behavior by DFT calculation(Fig. 13c and d).[84] And in order to improve accuracy, Kim *et al.* used the hybrid DFT calculations to predict the Li diffusion behavior.[85] The major diffusion behaviors included in-plane diffusion and out of plane diffusion (Fig. 13e). The large triangular-like pore formed by the sp and sp^2 hybridized carbon atoms in GDY facilitated the Li diffusion and improved the charge/discharge of Li-ion batteries.

The practical application of GDY as a high-efficiency lithium storage material in experiments was reported by Li *et al.* in 2015 (refs. [63] and [86]) (Fig. 13j and k). Comparing experimental data with the theoretical value of surface capacity, the value of experimental results was larger than the theoretical capacity of monolayer GDY (Fig. 13h-I and h-II), but smaller than the monolayer GDY in Fig. 13h-III. This result indicated that Li storage in multilayer GDY occurred mainly through both the interlayer insertion/extraction way (Fig. 13f) and surface adsorption/desorption method on the surface of the GDY films (Fig. 13g and i). Based on the above calculation research, the intrinsic advantages make GDY an ideal candidate for constructing electrode materials. Furthermore, GDY/MOs can

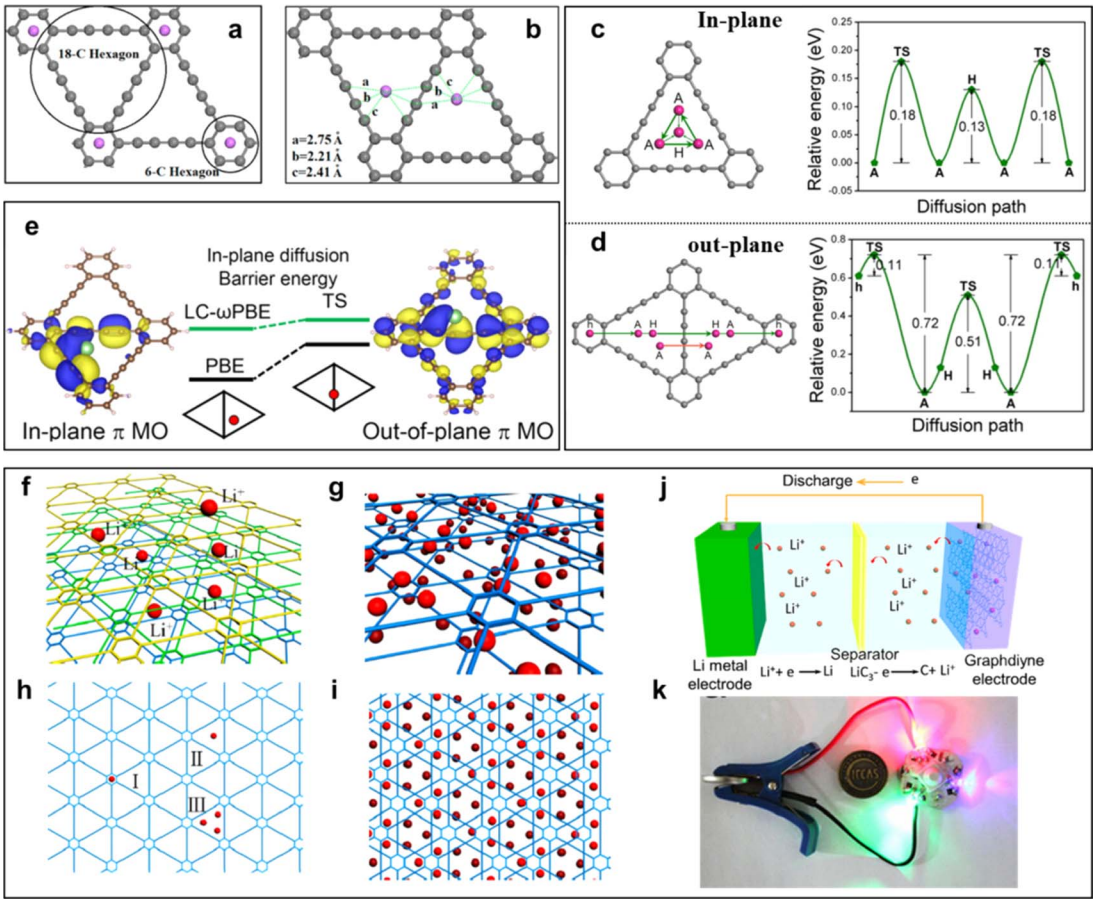

Fig. 13 (a) Li in 6-C hexagon (two Li atoms are distributed on the two sides of the carbon network) and (b) Li in 18-C hexagon (both Li atoms are on the same side of the carbon network);[83] (c) diffusion pathway of Li within one triangular-like pore and corresponding energy profile as a function of adsorption sites;[84] (d) diffusion pathways of Li and corresponding energy profiles as a function of adsorption sites across a GDY layer; (f) Li-intercalated GDY; (g) three different sites for occupation by Li atoms in GDY; adsorption of Li atoms on (h and i) both sides;[85] (j) representation of an assembled GDY-based battery; (k) photograph exhibition of the assembled full Li-ion battery and applied discharge for the lighting of an LED bulb. Li-storage of GDY in a Li-ion cell.[86]

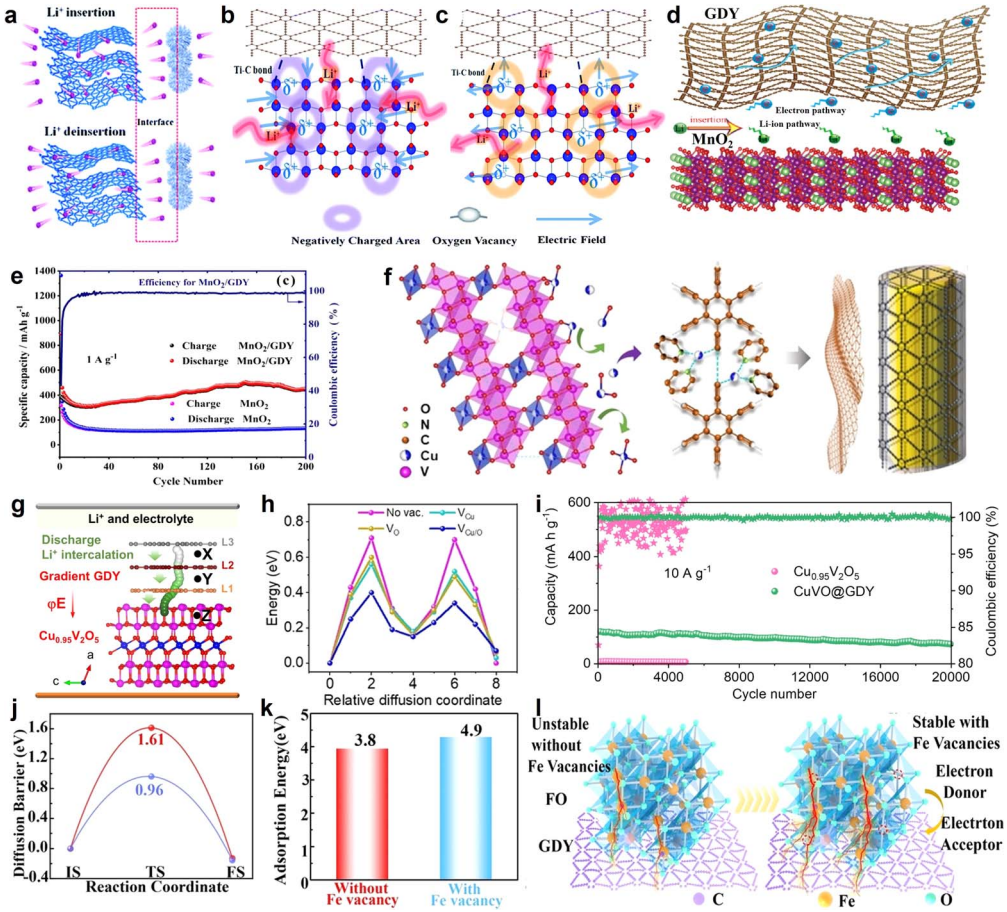

Fig. 14 (a) An interfacial built-in electric field (*E*) between TiO_2 and GDY, which facilitates charge transfer across the interface; (b) and (c) schematic illustration of the potential mechanism behind the improved electrochemical performances due to the oxygen vacancy derived local built-in electric field;[87] (d) hybrid nanostructured MnO_2 nanowire/GDY and the electron/Li-ion pathway;[88] (e) cycling performance at 1 A g^{-1} of MnO_2/GDY, MnO_2 electrodes;[88] (f) Cu ions migrate out of the $Cu_{0.95}V_2O_5$ bulk phase to form $V_{Cu/O}$;[89] (g) illustration of the Li (green atoms) diffusion pathway from gradient GDY to $Cu_{0.95}V_2O_5$ *via* a built-in electric field (*E*); (h) the Li-ion migration energy barrier in the $Cu_{0.95}V_2O_5$ bulk phase;[89] (i) cycling performance of $Cu_{0.95}V_2O_5$ and CuVO@GDY at a high current density of 10 A g^{-1};[89] (j) diffusion barrier without Fe vacancies and with Fe vacancies;[90] (k) Li adsorption energy without Fe vacancies and with Fe vacancies;[90] (l) the scheme of formation of Fe vacancy in the presence of GDY.[90]

improve interfacial ion and electron conductivities, and enhance the interfacial stability to realize the construction of high-efficiency electrodes. In 2018, the Huang group first reported the GDY/MOs, TiO_2@GDY, with superior electrochemical performances for lithium-ion batteries.[87] The results indicated that TiO_2@GDY showed a high reversible capacity of 432.4 mA h g^{-1} after 300 cycles at a current density of 1 A g^{-1}. It was about 3 times that of TiO_2. There were two main reasons why the TiO_2@GDY was so effective. One was the heterojunction interfaces (Fig. 14a), the built-in electric field could facilitate Li-ion diffusion from GDY to TiO_2, and different work functions brought about electron transfer from TiO_2 (~5.70 eV) to GDY (~4.52 eV). The same mechanism of heterojunction interfaces of MnO_2/GDY (Fig. 14d) was also reported by Huang's group after 2 years.[88] The research indicated that about 200 cycles later, the irreversible capacity was maintained at 450 mA h g^{-1} while the MnO_2 was just about 100 mA h g^{-1} (Fig. 14e). The vacancies can also significantly affect the performance of GDY/MOs. It not only provided more ion storage sites, but also facilitated the ion diffusion and improved the electrochemical reactivity and kinetics. For example, the local electric field produced by the oxygen-vacancies can further enhance the electrochemical performances of TiO_2@GDY (Fig. 14b and c). Recently, the dual-vacancy strategy for the $Cu_{0.95}V_2O_5$@-GDYcatalyst (Fig. 14f) was firstly reported by Li's group to enhance the fast-charging capability of lithium-ion batteries.[89] Compared to single V_{Cu} or V_o vacancy conditions, the lowest Li-ion migration energy barrier was achieved when dual-V_{Cu} and V_o were both present in the $Cu_{0.95}V_2O_5$@GDY catalyst (Fig. 14h). The $Cu_{0.95}V_2O_5$@GDY anodes with a built-in electric field (*E*) pointing from GDY to $Cu_{0.95}V_2O_5$ (Fig. 14g) showed high capacities of 120.3 mA h g^{-1} for 20 000 cycles at extremely high current densities of 10 Ag^{-1} (Fig. 14i). Besides the oxygen vacancy, the cationic vacancies also play a key role in modulating the electronic structure of electrode materials. For example, iron cationic vacancies (IV) of the GDY/ferroferric oxide heterostructure (IV-GDY-FO) were reported by Li's Group.[90] The charge transfer from FO to GDY could induce high

valence Fe and exist stably with Fe vacancy (Fig. 14l). Fe vacancies can decrease diffusion energy barrier (Fig. 14j) and improve adsorption energies (Fig. 14k), and accelerate the kinetic process to realize speedy charge transfer and ion diffusion.

4.2 Applications of GDY/MOs in environmental remediation

4.2.1 Air pollution control. With the interaction between GDY and MOs, GDY/MOs have strong CO adsorption and oxygen activation ability, which endow them with outstanding CO oxidation performance. Recently, our group firstly reported that the neighboring sp-hybridized C and Cu sites on sub-nanocluster CuO/GDY were the key structures to effectively modulate the O_2 activation process in the bridging adsorption mode for CO oxidation (Fig. 15a).[29] Compared to the sp^2-hybridized carbon materials (graphene), the unique diacetylene bonds (–C≡C–C≡C–) in GDY could promote the activation of molecular oxygen to produce more ROS (Fig. 15b, $\cdot O_2^-$). Furthermore, the neighboring sp-hybridized C is more favorable to promote the rapid dissociation of carbonate than sp^2-hybridized C, which facilitates the low-temperature CO oxidation. CuO/GDY can readily convert 50% CO at around 133 °C, which is 34 °C lower than that for CuO/graphene (Fig. 15c).

Moreover, our group has also made some progress in ozone (O_3) removal. O_3, as a greenhouse gas and secondary atmospheric pollutant, has caused serious harm to the ecosystem and human health. Therefore, efficient and rapid removal of O_3 is of great significance to the protection of environmental safety and human health. Recently, our group has reported a three-dimensional monolithic MoO_3/GDY catalyst with a C–O–Mo bond. The sp-C in GDY could donate electrons to MoO_3 through the C–O–Mo bond, which facilitated the activation of water to hydroxyl species (Fig. 15d), serving as the new active sites (MoO_3/GDY-2OH) for rapid and efficient O_3 decomposition under high humidity (RH = 75%).[8] And further, EPR spectroscopic experiments show that the MoO_3/GDY catalyst can accelerate O_3 decomposition and produce more active oxygen species ($\cdot OH$ and $\cdot O_2^-$) under humid conditions (Fig. 15e). As shown in Fig. 15f, MoO_3/GDY showed the best O_3 decomposition activity under high humidity conditions (75% RH) than control samples: Cu foam and GDY, MoO_3 and other carbon-based MoO_3 materials (MoO_3/CNTs, MoO_3/AC, MoO_3/GR). This study demonstrates the feasibility of water-promoted O_3 decomposition on GDY/MOs and provides new insights on the design of water activation for heterogeneous catalysis in a high-humidity atmosphere.

4.2.2 Liquid organic pollution control. In addition to gaseous pollutants, water pollution is also a serious risk to human health. GDY/MOs also demonstrate potential value in water treatment. The GDY possesses narrow band gap and high intrinsic charge mobility, which were utilized in the composites to improve the photocatalytic performance of MOs.[91] Moreover, the formation of reactive oxygen species such as $\cdot O_2^-$ and $\cdot OH$ due to the activation of water and oxygen on GDY/MOs can efficiently decompose the organic dye molecule into CO_2 and H_2O.[92] Venugopal *et al.* prepared the GDY–ZnO catalyst by the one-pot hydrothermal method and examined the effects on the photodegradation of methylene blue and rhodamine.[93] The experimental results demonstrated that the GDY–ZnO possessed superior photocatalytic efficiency for the degradation

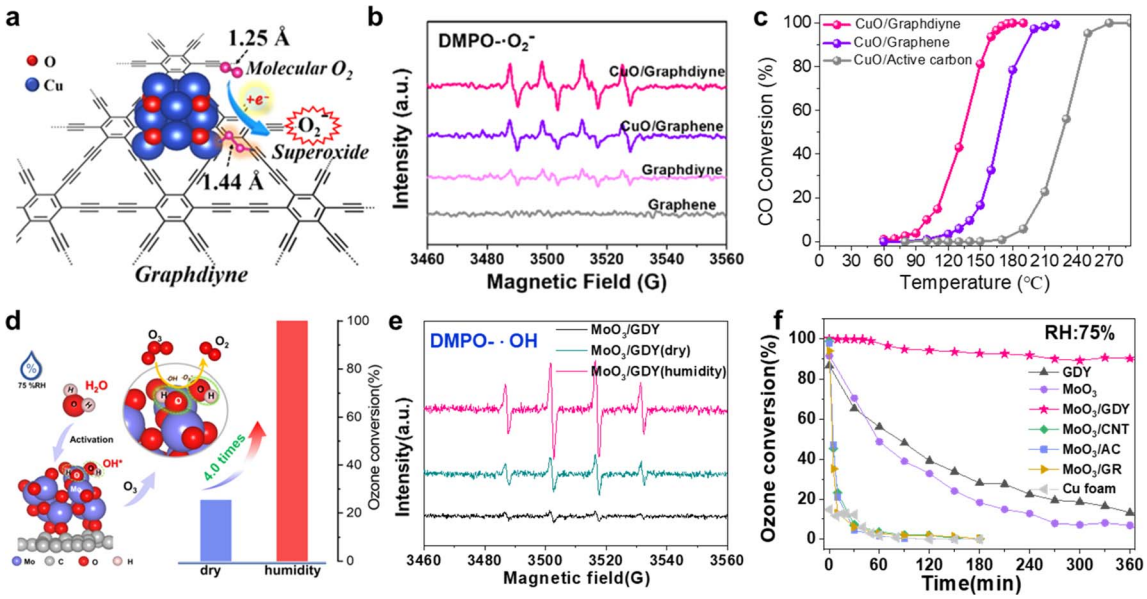

Fig. 15 (a) Neighboring sp-hybridized carbon-involved O_2 activation on the interface of sub-nanocluster CuO/GDY; (b) EPR spectra of CuO/GDY and GDY for $^{\bullet}\cdot O_2^-$ in DMPO spin trap solution; (c) light-off curves for CO oxidation over CuO/GDY, CuO/graphene, and CuO/active carbon samples [reaction conditions: 1% CO + 5% O_2/N_2 balanced, total flow rate of 25 mL min^{-1}, and WHSV = 10 000 mL (g^{-1} h^{-1})];[29] (d) rapid O_3 decomposition over water-activated monolithic MoO_3/GDY nanowalls under high humidity; (e) EPR spectra of pristine MoO_3/GDY, O_3-exposed MoO_3/GDY under dry and humid conditions for $^{\bullet}OH$ in DMPO spin trap solution; (f) the O_3 conversion of GDY, MoO_3, MoO_3/GDY, MoO_3/CNTs, MoO_3/AC, MoO_3/GR and Cu foam under humid conditions (75% RH).[8]

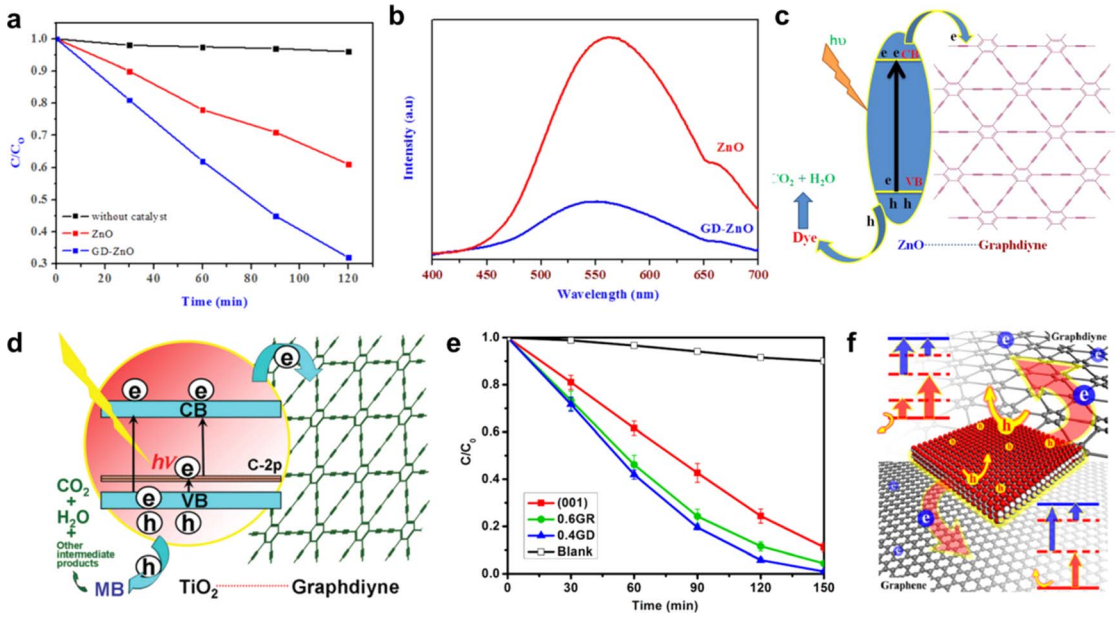

Fig. 16 (a) Photocatalytic performance of GDY–ZnO nanohybrids and ZnO nanoparticles in the degradation of methylene blue;[93] (b) photoluminescence spectra of ZnO and GDY–ZnO nanohybrids;[93] (c) schematic representation of GD-ZnO nanohybrid photocatalysis;[93] (d) schematic structure of P25-GD and tentative processes of the photodegradation of methylene blue (MB) over P25-GDY;[94] (e) photocatalytic degradation of MB over TiO_2(001), TiO_2(001)GDY, TiO_2(001)GR composites, and the blank experiment; (f) schematic of the photocatalytic properties of TiO_2-graphdiyne, and TiO_2-graphene composites.[95]

of dyes to that of bare ZnO (Fig. 16a). The absorption edge of ZnO decreased due to the induction of GDY in GDY–ZnO (Fig. 16b), thereby more photon energy was utilized, leading to an enhanced photocatalytic reaction rate. Furthermore, the conductive nature of GDY may make it a viable candidate for effective transfer of photogenerated electrons from ZnO to GDY, suppressing the recombination of free charge carriers (Fig. 16c). The trapped electron on GDY can react with dissolved oxygen to form $\cdot O_2^-$, whereas the holes react with water to form ·OH, which decomposed the azo dyes. Wang *et al.* prepared a series of chemically bonded titania(P25)-GDY nanocomposites which showed higher photocatalytic performance for degrading methylene blue than bare P25, P25-CNTs and P25-GR.[94] The formation of chemical bonds between P25 and GDY effectively decreased the bandgap of P25 and extended its absorbable light range. The introduction of a C 2p impurity band can contribute to the narrowing of the TiO_2 band. Moreover, GDY served as the acceptor of the photogenerated electrons of P25 and ensured fast charge transportation (Fig. 16d). Besides, Wang *et al.* compared the photocatalytic properties of TiO_2-graphdiyne, and TiO_2-graphene composites by first-principles density functional theory and experiment.[95] The TiO_2-graphdiyne composites possessed superior charge separation and oxidation properties (Fig. 16e and f), thereby they exhibited an oxidative degradation rate constant for methylene blue of 1.63 and 1.27 times that of pure TiO_2 and TiO_2-GR composites, respectively. The studies we discussed above all reveal the potential value of GDY/MOs for organic pollutants.

4.2.3 Antibacterial applications. The presence of bacterial and viruses poses a threat to human health and the environment.[96] GDY/MOs as an excellent photocatalytic material can produce numerous ROS to kill bacteria. In 2020, Zhang's group reported GDY-modified TiO_2 nanofibers with osteoinductive and enhanced photocatalytic antibacterial activities to prevent implant infection.[36] GDY and UV played a key role in the reaction. Compared to TiO_2 + UV, the ratio of dead cells to live cells in the TiO_2/GDY + UV group was much higher (4 times, Fig. 17a and b). The electron spin resonance (ESR) spectra further confirmed that the ROS (O_2^-, ·OH) generation ability was significantly enhanced after TiO_2 nanofibers were incorporated with GDY (Fig. 17c and d). In addition, our group has made decent progress in antimicrobials. We have fabricated a series of antimicrobial materials that exhibit excellent antimicrobial performance (CuO/TiO_2, Ag/CuO-V_o, Ag/GDY, CuO/GDY), and have investigated the mechanisms of bacteria inactivation in depth,[25,97–99] respectively. In particular, CuO/GDY exhibited outstanding *E. coli* inactivation activity. The *E. coli* inactivation efficiency of CuO/GDY was about 19 and 7.9 times that of GDY and CuO, respectively (Fig. 17e). The high energy acetylene bond of GDY not only effectively regulated the electronic structure of CuO, but prevented CuO nanoparticles from agglomerating into the bulk CuO. ESR results indicated that the CuO/GDY surface/interface can transfer electrons to molecular oxygen and effectively activated molecular oxygen to $\cdot O_2^-$ species (Fig. 17f), which could peroxidize the phospholipids of *E. coli* cell membranes, leading to the cell membrane dysfunction and cell death (Fig. 17g).[25] These findings demonstrated that the GDY/MOs are potential antimicrobial materials. However, the research on antibacterial activity over GDY/MOs is in the initial stage, and novel high-performance antibacterial materials and antibacterial mechanisms need to be further explored.

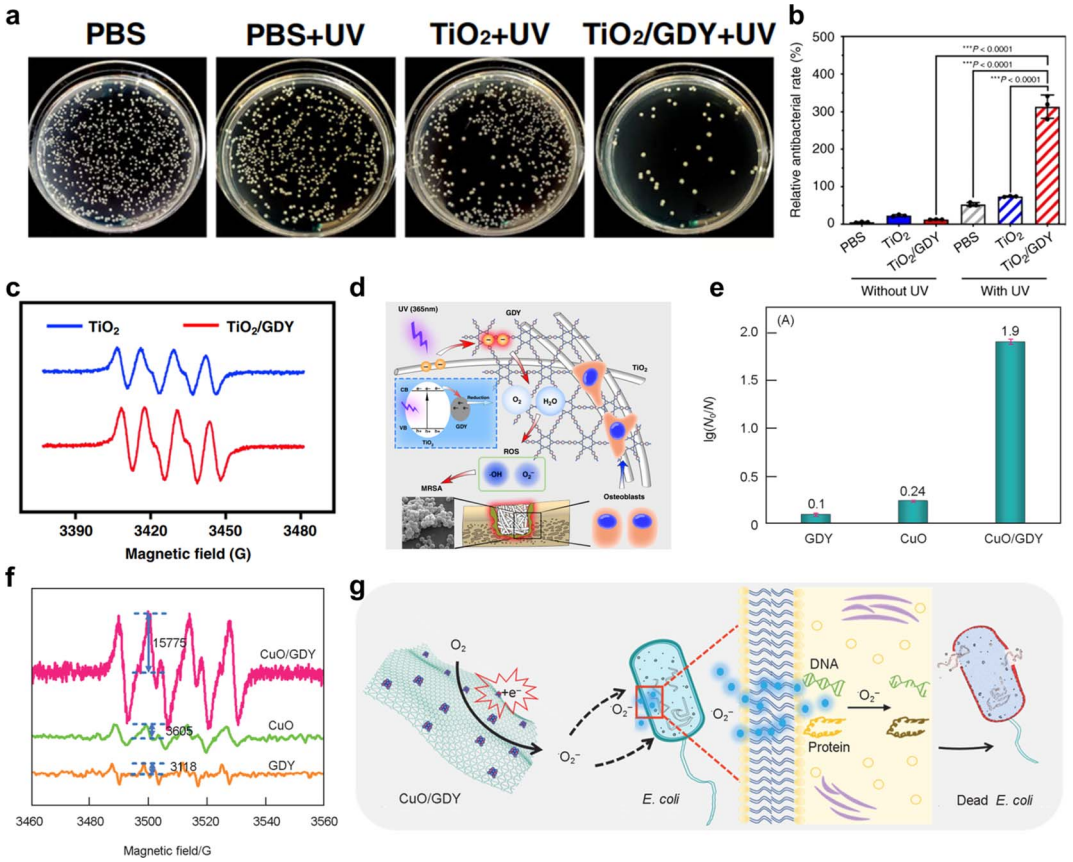

Fig. 17 (a)Photographs and quantitative analysis of the bacterial colonies of the infected femurs treated with TiO_2, TiO_2/GDY, or PBS as a control, with UV irradiation (365 nm, 2 W cm^{-1}, 5 min);[36] (b) semiquantification of the live/dead staining for the ratio of PI- and calcein AM-stained areas;[36] (c) ESR spectra of TiO_2, TiO_2/GDY for $^{\bullet}O_2^-$;[36] (d) schematic of the TiO_2/GDY in orthopedic implant infection, reactive oxygen species are produced in the process;[36] (e) *E. coli* inactivation efficiency of GDY, CuO and CuO/GDY;[25] (f) ESR spectra of GDY, CuO and CuO/GDY for $\cdot O_2^-$;[25] (g) illustration of the possible antibacterial mechanisms of CuO/GDY nanomaterials through oxidative stress.[25]

4.3 CO_2 reduction reaction

The depletion of fossil fuels and continued emissions of CO_2 have resulted in a growing energy and environmental crisis. The CO_2 reduction into chemical fuels is recognized as a potential solution to these issues.[100–105] At present, CO_2 reduction reactions (CO_2RR) mainly face the following challenges: (1) the CO_2 molecule is difficult to adsorb and activate; (2) hydrogen evolution reactions that compete with CO_2 reduction reactions should be effectively inhibited; (3) the stability of the catalyst needs to be improved; (4) the selectivity of reduction products is difficult to control and the mechanism of the CO_2 reduction reaction needs further study. To date, several attempts have been made to solve these problems.

Recently, Yu *et al.* successfully synthesized TiO_2 nanofibers supported by the GDY cocatalyst (Fig. 18a) through an electrostatic self-assembly method for photocatalytic CO_2 reduction.[106] The first calculations and *in situ* XPS tests showed that delocalized electrons in GDY can be hybridized with empty orbitals in TiO_2, forming an internal electric field (IEF) at the interfaces of TiO_2/GDY (Fig. 18b). The unique structure of IFE, combined with the photothermal effect of GDY, can enhance charge separation, directed electron transfer, CO_2 adsorption and activation (Fig. 18c–e), thus significantly improving the efficiency and selectivity of CO_2 photoreduction. Li *et al.* developed a GDY/SnO_x electrocatalyst with a novel heterostructure,[31] achieving highly selective reduction of CO_2 to formates at high current density. The results showed that GDY has advantages in effectively regulating the valence state of SnO_x, increasing the charge transfer ability and the number of active sites.

The maximum reaction selectivity was 99.5% and the formate yield was 323.42 μmol h^{-1} cm^{-2} at a high current density of 112 mA cm^{-2} and an applied voltage of −0.9 V *vs.* RHE. From the operando *in situ* infrared (IR) measurements, an upward peak at 1390 cm^{-1} indicated that the OCHO* species was the key intermediate in the formation of formate. And the appearance of *CO (1956 and 2012 cm^{-1}) explained the later emergence of CO. Combined with these results, they further proposed that the formation of OCHO* was an exothermic process while the formation of *COOH was endothermic conversely. Therefore, to generate formate, the limiting potential is determined by the OCHO* hydrogenation step. In conclusion, the conversion efficiency and the selectivity of target products can be improved by studying the mechanism of the CO_2RR deeply and designing efficient catalysts. In addition,

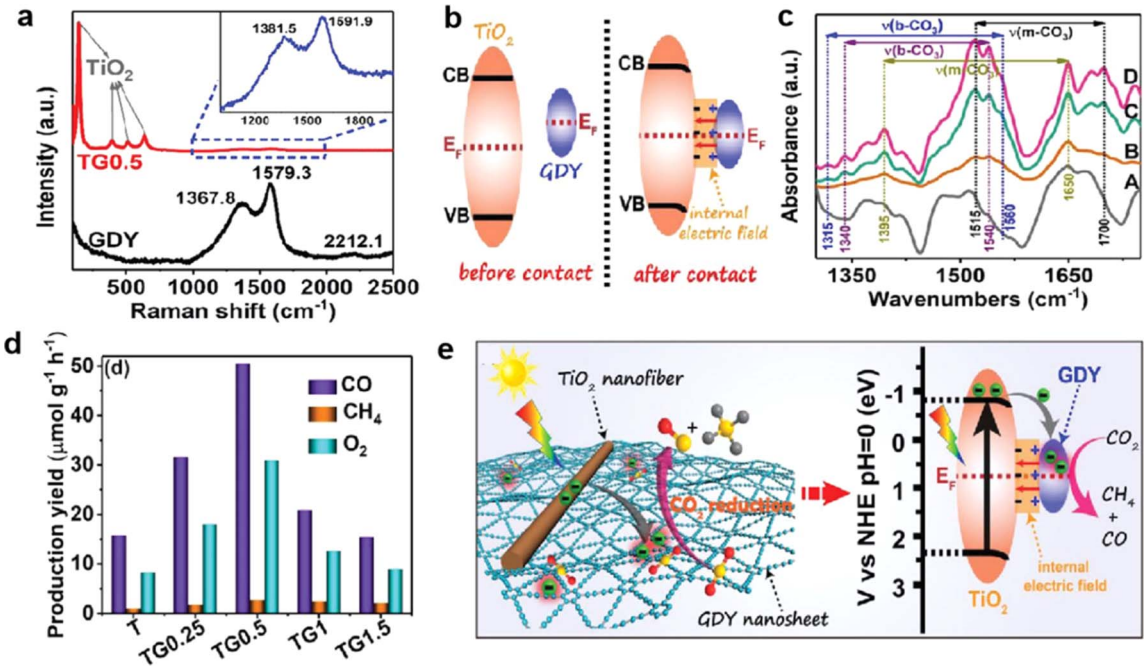

Fig. 18 $_2$ after adsorption of CO_2/H_2O for 60 min in dark (A) and TiO_2/GDY after adsorption of CO_2/H_2O for 20 (B), 40 (C), and 60 (D) min in dark; (a) Raman spectra of GDY and TiO_2/GDY; (b) schematic diagram for the electron transfer and the formation of IEF between TiO_2 and GDY upon their contact; (c) *in situ* DRIFTS spectra of TiO_2 after adsorption of CO_2/H_2O for 60 min in dark (A) and TiO_2/GDY after adsorption of CO_2/H_2O for 20 (B), 40 (C), and 60 (D) min in dark; (d) photocatalytic activities of CO_2 reduction over the samples; (e) schematic illustration of the TiO_2/GDY heterojunction: internal electric field-induced charge transfer and separation under UV-visible light irradiation for CO_2 photoreduction.[106]

photocatalytic conversion of CO_2 into energy-rich products is also an ideal strategy to pursue renewable energy;[103–105] GDY/MOs possess excellent CO_2 activation and charge separation/transfer ability and may be a potential photocatalytic CO_2 conversion material.

5. Conclusions and perspectives

In this review, we systematically summarized the structure, synthesis and advanced characterization methods of GDY/MOs and their applications in energy conversion and environmental remediation (HER, OER, NRR, CO_2RR, air pollution control, liquid organic pollution control, antibacterial activity, *etc.*). In particular, the detailed structure–performance relationship, activation behaviors (activation of H_2O, O_2, CO_2 and N_2), intermediate species and corresponding mechanisms for energy and environmental catalysis were discussed.

The unique sp-hybridized carbon atoms and triangular cavities in the GDY-conjugated structure facilitate the formation of strong interfacial contacts with metal oxide. The interaction between metal oxide and GDY endows GDY/MOs with fast charge transfer at the interface, promoting the adsorption and activation of reactant molecules (H_2O, N_2), and regulating the adsorption and desorption of active intermediates, which exhibits excellent performance in water electrolysis (HER and OER) and NRR. GDY as the carrier can disperse MOs uniformly and induce the formation of metal vacancy which could regulate the charge distribution around vacancies and adjacent atoms, facilitating electronic transportation, enlarging the lithium-ion diffusion, and thus displaying distinguished battery energy storage. The interfacial chemical bonds formed between sp-hybridized C and MOs endow GDY/MOs with the ability to activate oxygen to form $\cdot O_2^-$ species, enabling GDY to be used as an outstanding catalyst for low temperature CO oxidation and antimicrobial performance. The heterogeneous interfaces formed by high charge mobility GDY and MOs could generate more electron hole pairs under illumination, and effectively suppress the recombination of the generated electron–hole pairs, leading to excellent photocatalytic performance for carbon dioxide reduction, nitrogen reduction and degradation of organic pollutants such as methylene blue and rhodamine. Therefore, we believe that further exploration of GDY/MOs will further reveal their intrinsic properties and pave the way for practical applications in energy and environment-related fields.

The above unique advantages enable GDY/MOs to show excellent performance and great application potential in energy conversion and environmental remediation. Although many advances have been made in the synthesis and application of GDY/MOs for energy and environmental catalysis, the research and efficient utilization of GDY/MOs are still in the development stage and further improvements are still desired. Based on the current perspectives, it is worth carrying out more in-depth explorations into the synthesis, properties and practical applications in future research.

(i) The research of GDY/MOs is mainly focused on basic research. It is essential to explore the service life of the GDY/MOs and expand the practical applications in the fields of energy conversion and environmental remediation: (1)

exploring low-cost, large-scale, uniform and controllable synthesis of GDY/MOs; (2) assembling catalysts into device realizable applications, such as a complete set of devices directly capable of seawater electrolysis and a complete set of air purification device.

(ii) At present, the photocatalytic water splitting efficiency of GDY/MOs still needs to be improved. We can effectively choose GDY/MOs by DFT calculations and machine learning, and further enhance the photocatalytic water splitting performance by modulating the interfacial structure of GDY and suitable MOs.

(iii) Current research on GDY/MOs in the field of energy is mainly focused on water splitting and NH_3 synthesis. However, GDY can effectively transfer electrons to form strong interactions with MOs, which can promote the adsorption and activation of small molecules, and may have a greater application prospect in fuel cells and syngas preparation.

(iv) Besides CO and O_3, other gaseous pollutants also threaten the environment and human health, such as volatile organic compounds (VOCs). The strong interaction between acetylenic links in GDY and MOs can effectively activate O_2 and H_2O to generate $\cdot O_2^-$, $\cdot OH$, which has great potential for the oxidation of VOCs. Moreover, the catalytic mechanism of GDY/MOs for VOCs deserves in-depth and comprehensive exploration.

(v) Emerging pollutants (EPs) are a class of chemical pollutants that pose potential or substantial threats to human health and ecological environment. EPs mainly include pharmaceuticals and personal care products, endocrine disrupting chemicals, antibiotics, persistent organic pollutants, disinfection by-products and other industrial chemicals, *etc.* The GDY/MOs with high specific surface area and strong activation ability for organic pollutants can benefit the adsorption and elimination of some EPs.

(vi) Currently, the selectivity of the CO_2RR and NRR on GDY/MOs could reach nearly 100%, but its conversion rate is still very low, and it is necessary to continue to design and synthesize high-performance GDY/MO materials.

(vii) The relationship between the structures, properties, and performance of the GDY/MOs, active intermediates and mechanisms need to be thoroughly revealed and understood at the molecular and atomic levels through machine learning, and advanced *in situ* and *ex situ* techniques. At present, the research of GDY/MOs in energy and environmental catalysis is in its initial stage, there is still much room for improvement.

Undoubtedly, GDY/MOs are a key material for the development of high-performance and new technologies in the fields of energy conversion and environmental remediation. It is believed that GDY/MOs are capable of delivering incredible performance appropriate for the applications including but not limited to energy and environmental aspects. We are looking forward to a better tomorrow for GDY/MO research.

Author contributions

Y. Z., S. Z., Y. W. and Y. G. conceived the idea. Z. L. and Y. G supervised the project. The manuscript was written through the contributions of all authors.

Conflicts of interest

There are no conflicts to declare.

Acknowledgements

The authors gratefully acknowledge the financial support from the National Natural Science Foundation of China (grant number 22076060, 22376075), Natural Science Foundation for Distinguished Young Scholars of Hubei province (grant number 2021CFA085), Natural Science Foundation of Hubei Province, China (grant number 2022CFB321), The Recruitment Program of Global Young Experts start-up funds, The Program of Introducing Talents of Discipline to Universities of China (111 program, B17019), Longyan Major Science and Technology Project (2022LYF1006), and Knowledge Innovation Program of Wuhan Basic Research (2022010801020289).

References

1 S. De, J. Zhang, R. Luque and N. Yan, *Energy Environ. Sci.*, 2016, **9**, 3314–3347.
2 B. Song, M. Chen, G. Zeng, J. Gong, M. Shen, W. Xiong, C. Zhou, X. Tang, Y. Yang and W. Wang, *J. Hazard. Mater.*, 2020, **398**, 122957.
3 M. Li, N. Han, X. Zhang, S. Wang, M. Jiang, A. Bokhari, W. Zhang, M. Race, Z. Shen, R. Chen, M. Mubashir, K. S. Khoo, S. S. Teo and P. L. Show, *Environ. Res.*, 2022, **205**, 544.
4 Y. Zhu, Y. Yao, Z. Luo, C. Pan, J. Yang, Y. Fang, H. Deng, C. Liu, Q. Tan, F. Liu and Y. Guo, *Molecules*, 2019, **25**, 18.
5 Z. Zuo, D. Wang, J. Zhang, F. Lu and Y. Li, *Adv. Mater.*, 2018, **31**, 1803762.
6 G. Zhu, W. Zhu, Y. Lou, J. Ma, W. Yao, R. Zong and Y. Zhu, *Nat. Commun.*, 2021, **12**, 4152.
7 Q. Hao, Z. Li, Y. Shi, R. Li, Y. Li, S. Ouyang, H. Yuan and T. Zhang, *Nano Energy*, 2022, **102**, 107723.
8 Y. Zhu, L. Yang, J. Ma, Y. Fang, J. Yang, X. Chen, J. Zheng, S. Zhang, W. Chen, C. Pan, B. Zhang, X. Qiu, Z. Luo, J. Wang and Y. Guo, *Angew. Chem., Int. Ed.*, 2023, e202309158.
9 B. Li, C. Lai, M. Zhang, G. Zeng, S. Liu, D. Huang, L. Qin, X. Liu, H. Yi, F. Xu, N. An and L. Chen, *Adv. Energy Mater.*, 2020, **10**, 2000177.
10 X. Zheng, S. Chen, J. Li, H. Wu, C. Zhang, D. Zhang, X. Chen, Y. Gao, F. He, L. Hui, H. Liu, T. Jiu, N. Wang, G. Li, J. Xu, Y. Xue, C. Huang, C. Chen, Y. Guo, T. B. Lu, D. Wang, L. Mao, J. Zhang, Y. Zhang, L. Chi, W. Guo, X. H. Bu, H. Zhang, L. Dai, Y. Zhao and Y. Li, *ACS Nano*, 2023, **17**, 14309–14346.
11 Y. Fang, Y. Liu, L. Qi, Y. Xue and Y. Li, *Chem. Soc. Rev.*, 2022, **51**, 2681–2709.
12 S. Chai, X. Chen, X. Zhang, Y. Fang, R. S. Sprick and X. Chen, *Environ. Sci.: Nano*, 2022, **9**, 2464–2469.
13 M. Wang, M. Wang, H. H. Lin, M. Ballabio, H. Zhong, M. Bonn, S. Zhou, T. Heine, E. Canovas, R. Dong and X. Feng, *J. Am. Chem. Soc.*, 2020, **142**, 21622–21627.

14 Y. Fang, Y. Hou, X. Fu and X. Wang, *Chem. Rev.*, 2022, **122**, 4204–4256.
15 X. Gao, H. Liu, D. Wang and J. Zhang, *Chem. Soc. Rev.*, 2019, **48**, 908–936.
16 J. Liu, Q. Ma, Z. Huang, G. Liu and H. Zhang, *Adv. Mater.*, 2019, **31**, e1800696.
17 X. Chen, X. Jiang and N. Yang, *Small*, 2022, **18**, e2201135.
18 Y. Xue, B. Huang, Y. Yi, Y. Guo, Z. Zuo, Y. Li, Z. Jia, H. Liu and Y. Li, *Nat. Commun.*, 2018, **9**, 1460.
19 C. Pan, C. Wang, Y. Fang, Y. Zhu, H. Deng and Y. Guo, *Environ. Sci.: Nano*, 2021, **8**, 1863–1885.
20 J. Liu, C. Chen and Y. Zhao, *Adv. Mater.*, 2019, **31**, e1804386.
21 Y. Cao, X. Hao, X. Guo, K. Wang, G. Wang and Z. Jin, *Ind. Eng. Chem. Fundam.*, 2021, **60**, 18397–18407.
22 Y. Yao, Y. Zhu, C. Pan, C. Wang, S. Hu, W. Xiao, X. Chi, Y. Fang, J. Yang, H. Deng, S. Xiao, J. Li, Z. Luo and Y. Guo, *J. Am. Chem. Soc.*, 2021, **143**, 8720–8730.
23 J. Tang, M. Zhao, X. Cai, L. Liu, X. Li and T. Jiu, *Chem. Res. Chin. Univ.*, 2021, **37**, 1309–1316.
24 X. Luan, Z. Zheng, S. Zhao, Y. Xue and Y. Li, *Adv. Funct. Mater.*, 2022, **32**, 2202843.
25 C. Pan, X. Liu, X. Zhang, F. Mao, P. Xu, Y. Zhu, H. Deng, Z. Luo, H. Sun, L. Zhang and Y. Guo, *Chem. Res. Chin. Univ.*, 2021, **37**, 1341–1347.
26 S. Zhang and X. Wang, *Acc. Mater. Res.*, 2022, **3**, 1285–1298.
27 Q. Hu, K. Gao, X. Wang, H. Zheng, J. Cao, L. Mi, Q. Huo, H. Yang, J. Liu and C. He, *Nat. Commun.*, 2022, **13**, 3958.
28 M. Peng, C. Dong, R. Gao, D. Xiao, H. Liu and D. Ma, *ACS Cent. Sci.*, 2021, **7**, 262–273.
29 C. Pan, C. Wang, X. Zhao, P. Xu, F. Mao, J. Yang, Y. Zhu, R. Yu, S. Xiao, Y. Fang, H. Deng, Z. Luo, J. Wu, J. Li, S. Liu, S. Xiao, L. Zhang and Y. Guo, *J. Am. Chem. Soc.*, 2022, **144**, 4942–4951.
30 L. Liu and A. Corma, *Chem. Rev.*, 2018, **118**, 4981–5079.
31 X. Chen, X. Zheng, C. Zhang, D. Zhang, Y. Gao, S. Chen, Y. Xue and Y. Li, *Nano Energy*, 2023, **114**, 108622.
32 S. C. Shekar and R. S. Swathi, *J. Phys. Chem. C*, 2015, **119**, 8912–8923.
33 Z. Chen, Z. Wen and Q. Jiang, *J. Phys. Chem. C*, 2017, **121**, 3463–3468.
34 J. He, S. Y. Ma, P. Zhou, C. X. Zhang, C. He and L. Z. Sun, *J. Phys. Chem. C*, 2012, **116**, 26313–26321.
35 Z. Jin, X. Wang, X. Hao, G. Wang, X. Guo and K. Wang, *2D Mater.*, 2022, **9**, 025014.
36 R. Wang, M. Shi, F. Xu, Y. Qiu, P. Zhang, K. Shen, Q. Zhao, J. Yu and Y. Zhang, *Nat. Commun.*, 2020, **11**, 4465.
37 Y. Liu, Y. Xue, L. Hui, H. Yu, Y. Fang, F. He and Y. Li, *Nano Energy*, 2021, **89**, 106333.
38 X. Luan, L. Qi, Z. Zheng, S. Zhao, Y. Gao, Y. Xue and Y. Li, *Chem. Commun.*, 2023, **59**, 7611–7614.
39 Z. Wang, Z. Zheng, Y. Xue, F. He and Y. Li, *Adv. Energy Mater.*, 2021, **11**, 2101138.
40 J. Zhou, X. Gao, R. Liu, Z. Xie, J. Yang, S. Zhang, G. Zhang, H. Liu, Y. Li, J. Zhang and Z. Liu, *J. Am. Chem. Soc.*, 2015, **137**, 7596–7599.
41 F. Wang, Z. Zuo, L. Li, F. He, F. Lu and Y. Li, *Adv. Mater.*, 2019, **31**, 1806272.
42 Z. Luo, R. Miao, T. D. Huan, I. M. Mosa, A. S. Poyraz, W. Zhong, J. E. Cloud, D. A. Kriz, S. Thanneeru, J. He, Y. Zhang, R. Ramprasad and S. L. Suib, *Adv. Energy Mater.*, 2016, **6**, 1600528.
43 Q. Wei, C. Yu, X. Song, Y. Zhong, L. Ni, Y. Ren, W. Guo, J. Yu and J. Qiu, *J. Am. Chem. Soc.*, 2021, **143**, 6071–6078.
44 X. Zhang, F. Bi, Z. Zhu, Y. Yang, S. Zhao, J. Chen, X. Lv, Y. Wang, J. Xu and N. Liu, *Appl. Catal., B*, 2021, **297**, 120393.
45 S. Chen, Z. Zhang, W. Jiang, S. Zhang, J. Zhu, L. Wang, H. Ou, S. Zaman, L. Tan, P. Zhu, E. Zhang, P. Jiang, Y. Su, D. Wang and Y. Li, *J. Am. Chem. Soc.*, 2022, **144**, 12807–12815.
46 X. Niu, Q. Tang, B. He and P. Yang, *Electrochim. Acta*, 2016, **208**, 180–187.
47 J. Saavedra, C. J. Pursell and B. D. Chandler, *J. Am. Chem. Soc.*, 2018, **140**, 3712–3723.
48 J. Zhang, C. Muck-Lichtenfeld and A. Studer, *Nature*, 2023, **619**, 506–513.
49 Y. Wang, Y. Qu, B. Qu, L. Bai, Y. Liu, Z. D. Yang, W. Zhang, L. Jing and H. Fu, *Adv. Mater.*, 2021, **33**, e2105482.
50 L. Xiang, L. Zhang, J. Shao, F. Lin, Z. Wang, B. Yan and G. Chen, *J. Hazard. Mater.*, 2023, **441**, 129997.
51 H. Gu, X. Liu, X. Liu, C. Ling, K. Wei, G. Zhan, Y. Guo and L. Zhang, *Nat. Commun.*, 2021, **12**, 5422.
52 L. Kang, B. Wang, Q. Bing, M. Zalibera, R. Buchel, R. Xu, Q. Wang, Y. Liu, D. Gianolio, C. C. Tang, E. K. Gibson, M. Danaie, C. Allen, K. Wu, S. Marlow, L. D. Sun, Q. He, S. Guan, A. Savitsky, J. J. Velasco-Velez, J. Callison, C. W. M. Kay, S. E. Pratsinis, W. Lubitz, J. Y. Liu and F. R. Wang, *Nat. Commun.*, 2020, **11**, 4008.
53 X. P. Zhang, A. Chandra, Y. M. Lee, R. Cao, K. Ray and W. Nam, *Chem. Soc. Rev.*, 2021, **50**, 4804–4811.
54 Y. Mao, P. Wang, L. Li, Z. Chen, H. Wang, Y. Li and S. Zhan, *Angew. Chem., Int. Ed.*, 2020, **59**, 3685–3690.
55 Y. Du, W. Zhou, J. Gao, X. Pan and Y. Li, *Acc. Chem. Res.*, 2020, **53**, 459–469.
56 M. Li, Q. Lv, W. Si, Z. Hou and C. Huang, *Angew. Chem., Int. Ed.*, 2022, **61**, e202208238.
57 Y. Guo, J. Liu, Q. Yang, L. Ma, Y. Zhao, Z. Huang, X. Li, B. Dong, X. Z. Fu and C. Zhi, *Small*, 2020, **16**, e1907341.
58 Q. Lv, W. Si, J. He, L. Sun, C. Zhang, N. Wang, Z. Yang, X. Li, X. Wang, W. Deng, Y. Long, C. Huang and Y. Li, *Nat. Commun.*, 2018, **9**, 3376.
59 C. Huang, Y. Li, N. Wang, Y. Xue, Z. Zuo, H. Liu and Y. Li, *Chem. Rev.*, 2018, **118**, 7744–7803.
60 T. Lu, X. Hu, J. He, R. Li, J. Gao, Q. Lv, Z. Yang, S. Cui and C. Huang, *Nano Energy*, 2021, **85**, 106024.
61 L. Qi, Z. Zheng, C. Xing, Z. Wang, X. Luan, Y. Xue, F. He and Y. Li, *Adv. Funct. Mater.*, 2022, **32**, 2107179.
62 Y. Fang, Y. Xue, L. Hui, H. Yu, C. Zhang, B. Huang and Y. Li, *Adv. Sci. (Weinh)*, 2022, **9**, e2102721.
63 C. Huang, S. Zhang, H. Liu, Y. Li, G. Cui and Y. Li, *Nano Energy*, 2015, **11**, 481–489.
64 A. Pei, R. Xie, Y. Zhang, Y. Feng, W. Wang, S. Zhang, Z. Huang, L. Zhu, G. Chai, Z. Yang, Q. Gao, H. Ye, C. Shang, B. H. Chen and Z. Guo, *Energy Environ. Sci.*, 2023, **16**, 1035–1048.

65 Y. Yao, Z. Jin, Y. Chen, Z. Gao, J. Yan, H. Liu, J. Wang, Y. Li and S. Liu, *Carbon*, 2018, **129**, 228–235.
66 R. Samanta, B. K. Manna, R. Trivedi, B. Chakraborty and S. Barman, *Chem. Sci.*, 2024, **15**, 364–378.
67 Q. Liu, Z. Yan, J. Gao, H. Fan, M. Li and E. Wang, *Chem. Sci.*, 2023, **14**, 11830–11839.
68 H. Yu, Y. Xue, L. Hui, F. He, C. Zhang, Y. Liu, Y. Fang, C. Xing, Y. Li, H. Liu and Y. Li, *Nano Energy*, 2019, **64**, 103928.
69 C. Zhang, Y. Xue, L. Hui, Y. Fang, Y. Liu and Y. Li, *Mater. Chem. Front.*, 2021, **5**, 5305–5311.
70 L. Hui, Y. Xue, B. Huang, H. Yu, C. Zhang, D. Zhang, D. Jia, Y. Zhao, Y. Li, H. Liu and Y. Li, *Nat. Commun.*, 2018, **9**, 5309.
71 J. Li, X. Han, D. Wang, L. Zhu, M. H. Ha-Thi, T. Pino, J. Arbiol, L. Z. Wu and M. Nawfal Ghazzal, *Angew. Chem., Int. Ed.*, 2022, **61**, e202210242.
72 Y. Gao, Y. Xue, F. He and Y. Li, *Proc. Natl. Acad. Sci. U. S. A.*, 2022, **119**, e2206946119.
73 Q. Hao, Y. Song, H. Ji, Z. Mo, X. She, J. Deng, T. Muhmood, X. Wu, S. Yuan, H. Xu and H. Li, *Appl. Surf. Sci.*, 2018, **459**, 845–852.
74 H. Y. Lin, Z. X. Lou, Y. Ding, X. Li, F. Mao, H. Y. Yuan, P. F. Liu and H. G. Yang, *Small Methods*, 2022, **6**, e2201130.
75 J. Li, X. Gao, L. Zhu, M. N. Ghazzal, J. Zhang, C.-H. Tung and L.-Z. Wu, *Energy Environ. Sci.*, 2020, **13**, 1326–1346.
76 X. Luan and Y. Xue, *Chem. Res. Chin. Univ.*, 2021, **37**, 1268–1274.
77 M. A. Légaré, G. Bélanger-Chabot, R. D. Dewhurst, E. Welz, I. Krummenacher, B. Engels and H. Braunschweig, *Science*, 2018, **359**, 896–900.
78 T.-N. Ye, S.-W. Park, Y. Lu, J. Li, M. Sasase, M. Kitano, T. Tada and H. Hosono, *Nature*, 2020, **583**, 391–395.
79 H. Yu, L. Hui, Y. Xue, Y. Liu, Y. Fang, C. Xing, C. Zhang, D. Zhang, X. Chen, Y. Du, Z. Wang, Y. Gao, B. Huang and Y. Li, *Nano Energy*, 2020, **72**, 104667.
80 X. Wang, X. Hu, L. Zheng, Q. Lv, J. He, X. Li, R. Li, T. Lu and C. Huang, *Nano Energy*, 2023, **117**, 108919.
81 X. Gao, J. Li, R. Du, J. Zhou, M.-Y. Huang, R. Liu, J. Li, Z. Xie, L.-Z. Wu, Z. Liu and J. Zhang, *Adv. Mater.*, 2017, **29**, 1605308.
82 Y. Fang, Y. Xue, L. Hui, H. Yu and Y. Li, *Angew. Chem., Int. Ed.*, 2020, **60**, 3170–3174.
83 C. Sun and D. J. Searles, *J. Phys. Chem. C*, 2012, **116**, 26222–26226.
84 H. Zhang, Y. Xia, H. Bu, X. Wang, M. Zhang, Y. Luo and M. Zhao, *J. Appl. Phys.*, 2013, **113**, 044309.
85 J. Kim, S. Kang, J. Lim and W. Y. Kim, *ACS Appl. Mater. Interfaces*, 2019, **11**, 2677–2683.
86 S. Zhang, H. Liu, C. Huang, G. Cui and Y. Li, *Chem. Commun.*, 2015, **51**, 1834–1837.
87 Z. Lin, G. Liu, Y. Zheng, Y. Lin and Z. Huang, *J. Mater. Chem. A*, 2018, **6**, 22655–22661.
88 Y. Lin, H. Kang, M. Liang, X. Ye, J. Li, Q. Feng, Y. Zheng and Z. Huang, *Appl. Surf. Sci.*, 2020, 526.
89 F. Wang, J. An, H. Shen, Z. Wang, G. Li and Y. Li, *Angew. Chem., Int. Ed.*, 2023, **62**, e202216397.
90 M. Luo, J. Yang, X. Li, M. Eguchi, Y. Yamauchi and Z.-L. Wang, *Chem. Sci.*, 2023, **14**, 3400–3414.
91 Q. Peng, J. Crean, L. Han, S. Liu, X. Wen, S. De and A. Dearden, *Nanotechnol., Sci. Appl.*, 2014, **7**, 1–29.
92 A. Kubacka, M. Fernández-García and G. Colón, *Chem. Rev.*, 2011, **112**, 1555–1614.
93 S. Thangavel, K. Krishnamoorthy, V. Krishnaswamy, N. Raju, S. J. Kim and G. Venugopal, *J. Phys. Chem. C*, 2015, **119**, 22057–22065.
94 S. Wang, L. Yi, J. E. Halpert, X. Lai, Y. Liu, H. Cao, R. Yu, D. Wang and Y. Li, *Small*, 2011, **8**, 265–271.
95 N. Yang, Y. Liu, H. Wen, Z. Tang, H. Zhao, Y. Li and D. Wang, *ACS Nano*, 2013, **7**, 1504–1512.
96 Q. Bai, H. Luo, S. Shi, S. Liu, L. Wang, F. Du, Z. Yang, Z. Zhu and N. Sui, *J. Colloid Interface Sci.*, 2022, **613**, 376–383.
97 G. Liu, Z. Hu, X. Chen, W. Li, Y. Wu, Z. Liu, L. Miao, Z. Luo, J. Wang and Y. Guo, *J. Hazard. Mater.*, 2023, **465**, 133269.
98 C. Pan, B. Zhang, T. Pan, H. Huang, S. Song, X. Cai, Y. Wang, H. Sun, Z. Luo, L. Zhang and Y. Guo, *Environ. Sci.: Nano*, 2023, **10**, 3072–3083.
99 C. Pan, H. Shen, G. Liu, X. Zhang, X. Liu, H. Liu, P. Xu, W. Chen, Y. Tian, H. Deng, H. Sun, J. Wang, Z. Luo, L. Zhang and Y. Guo, *ACS Appl. Nano Mater.*, 2022, **5**, 10980–10990.
100 S. Sorcar, Y. Hwang, C. A. Grimes and S.-I. In, *Mater. Today*, 2017, **20**, 507–515.
101 S. Cao, B. Shen, T. Tong, J. Fu and J. Yu, *Adv. Funct. Mater.*, 2018, **28**, 1800136.
102 Z. Zeng, Y. Yan, J. Chen, P. Zan, Q. Tian and P. Chen, *Adv. Funct. Mater.*, 2018, **29**, 1806500.
103 Y. Wang, Y. Liu, L. Tan, X. Lin, Y. Fang, X. F. Lu, Y. Hou, G. Zhang and S. Wang, *J. Mater. Chem.*, 2023, **11**, 26804–26811.
104 B. Su, M. Zheng, W. Lin, X. F. Lu, D. Luan, S. Wang and X. W. Lou, *Adv. Energy Mater.*, 2023, **13**, 2203290.
105 B. Su, Y. Kong, S. Wang, S. Zuo, W. Lin, Y. Fang, Y. Hou, G. Zhang, H. Zhang and X. Wang, *J. Am. Chem. Soc.*, 2023, **145**, 27415–27423.
106 F. Xu, K. Meng, B. Zhu, H. Liu, J. Xu and J. Yu, *Adv. Funct. Mater.*, 2019, **29**, 1904256.